Structure-Property Relationships of 3D Printed Thermoplastics for Implantable Orthopedic Devices

by

Natalia von Windheim

Department of Mechanical Engineering and Materials Science
Duke University

Date:_____

Approved:

_____
Kenneth Gall, Advisor

_____
L. Catherine Brinson

_____
John E. Dolbow

_____
Christine K. Payne

Dissertation submitted in partial fulfillment of
the requirements for the degree of Doctor
of Philosophy in the Department of
Mechanical Engineering and Materials Science in the Graduate School
of Duke University

2021

ABSTRACT

Mechanical Properties of 3D Printed Thermoplastics for Implantable Orthopedic Devices

by

Natalia von Windheim

Department of Mechanical Engineering and Materials Science
Duke University

Date:_____

Approved:

_____
Kenneth Gall, Advisor

_____
L. Catherine Brinson

_____
John E. Dolbow

_____
Christine K. Payne

An abstract of a dissertation submitted in partial
fulfillment of the requirements for the degree
of Doctor of Philosophy in the Department of
Mechanical Engineering and Materials Science in the Graduate School of
Duke University

2021

Abstract

3D printing is a promising new technology with the potential to create rapid, high-quality, durable custom implants that will provide physicians and patients with currently unattainable clinical solutions. However, it is falling short on its promise due to its inability achieve adequate mechanical properties compared to conventional manufacturing techniques. This work explores the structure and properties of 3D printed thermoplastics with relevant medical applications through fused filament fabrication (FFF) processing. Four FFF materials (PLA, PEEK, PEKK, and PPSU) are investigated with an emphasis on characterizing printed weld formation and the corresponding mechanical properties. Each material has properties that are suitable for varying applications, but a pervasive requirement for success is strong weld formation between printed layers. Weld formation and strength was tested through tensile testing of bulk samples with layers oriented perpendicular to loading direction and tear testing of individual welds. While PLA, PEEK, and PEKK derive strength from their crystalline structures, crystallinity that developed during printing decreased the strength of materials as it inhibited polymer diffusion across the weld and prevented strong bonds from forming. Increasing crystallinity of as-printed amorphous samples through annealing did not result in higher strength for PLA or PEEK, due to the inability to co-crystallize across the weld interface. However, annealing amorphous PEKK samples

resulted in a 26-40% increase in strength. While PEKK achieved the highest strength of 105 MPa, PPSU, a completely amorphous material, was closest to achieving conventional processing properties with a strength of 61 MPa.

Contents

List of Tables

List of Figures

Acknowledgements

There are many people I would like to acknowledge for their contributions and support in completing my dissertation. First, my advisor, Ken Gall. Of course, my PhD would not be possible without Ken's advising and support, but there were many ways his teaching expanded outside the technical aspects of my PhD to applications of basic research and mentoring and teaching others. I am very grateful for the many opportunities afforded to me during my time at Duke and the continuous support I received. I am also grateful for the other members of the Gall Research Group including Alina Kirillova, Bijan Abar, Emilio Bachitar, Cambre Kelly, and Katie Nelson.

Next, I would like to acknowledge my committee members, L. Catherine Brinson, Christine K. Payne, and John E. Dolbow for their valuable feedback on my research and for the additional ways they mentored me as a TA and through my involvement with the Duke MEMS Graduate Student Committee. In particular, I am thankful for the collaboration that developed with Cate Brinson's lab through this project. In particular, I would like to thank David Collinson for his contributions to this work and for making the time in the lab preparing samples much more enjoyable.

There are many undergrads that completed work that contributed to this research including Trent Lau, Iman von Briesen, Tiffany Wu and Harrison Park. I am grateful for all of their hard work and the experience I gained through mentoring them.

Especially to Trent who worked with my through some of the most challenging aspects of this research.

This research would have not been possible without the support from restor3d and the wonderful people that work there. I would like to thank Tim Govert for his help with printing samples and Nathan Evans for his knowledgeable feedback and insight on this project and potential applications. Additionally, the access to their 3D printers and lab space was essential for completing this work.

Finally, I would like to thank my family and friends for their emotional and moral support along the way. To my mom and dad for their continuous encouragement that drove me to pursue a PhD and carried me the whole way through. And to Curtis, for being there for me in any and every way.

1. Introduction

The following sections include the motivation for exploring the structure-property relationships of 3D printed thermoplastics for orthopedic devices and the research objectives set to develop an understanding of the structure-property relationship.

1.1 Motivation

As 3D printers have grown in popularity, the promise of them revolutionizing traditional polymeric manufacturing methods has grown as well. Traditional manufacturing is optimized for identical devices at large production quantities; however, additive manufacturing, also referred to as 3D printing, has specific strengths in rapid prototyping, custom parts, and complex assemblies and geometries. These applications are either more costly or impossible due to complexity with traditional manufacturing. Unfortunately, 3D printing is falling short on its promise due to anisotropic mechanical properties. The layer by layer nature of 3D printing creates weak interfaces known as welds. Mechanical properties are sometimes reduced by over 50% when testing direction is perpendicular to welds, depending on material and processing method. There is a significant demand for the custom and complex nature of 3D printed products in the medical industry. However, when medical devices have mechanical property requirements, there are limited products on the market due to a poor understanding of the 3D printing processing-structure-property relationship.

For thermoplastics, there are two primary methods of 3D printing that involve melting and reforming the plastic – fused filament fabrication and selective laser sintering. Fused filament fabrication (FFF, also known as fused deposition modeling FDM) is extrusion based with a plastic filament fed into a hotend fixed to moving axes which it is fed into, melted, and extruded through a nozzle. Powder bed fusion (PBF) is a powder bed printing method which a bed of polymer powder is selectively sintered together by a laser in a layer-by-layer fashion. A couple challenges with PBF are the expense of machine and the potential waste from unsintered powder in the bed that cannot be reused. There is ongoing research relating to reuse of the unsintered powder but current research shows changes in the powder and a decrease in properties when using recycled powder. In general, FFF is a cheaper, more common and accessible method and the one explored in this research.

1.2 Research Objectives

The goal of this research is to evaluate the mechanical properties of FFF thermoplastics for high strength implantable orthopedic devices and determine areas for improvement with a focus on the welds that form between layers during FFF processing. Thermoplastics with a history of use in orthopedic devices were selected for evaluation including PLA, PEEK, PEKK, and PPSU. Print processing and post process annealing parameters were analyzed to determine impact on the structure and properties of printed parts.

Aim 1 – Understand impact of printing process parameters and post process annealing on mechanical anisotropy and weld strength of 3D printed PLA

PLA is one of the most common printed and investigated materials for 3D printing. We used this material to start our investigation as it is, like PEEK, a semicrystalline thermoplastic and has a history of use in orthopedic implants. There is also a larger amount of literature provided more context for experimentation and results. Key printing parameters of layer height and print speed were selected and related to porosity and crystallinity of the printed part to investigate how changing the process parameters impacted the tensile strength. The print orientation of samples was tested to create print layers that were parallel and perpendicular to tensile loading direction. Additionally, samples were annealed after printing to determine if properties can be improved post-printing through decreasing porosity or increasing crystallinity.

Aim 2 – Investigate influence of print processing conditions and post-process annealing on weld formation and tear and tensile properties of PEEK

PEEK crystallization during printing was studied by printing singled-walled cylinders and changing the build chamber temperature from a minimum of 70 °C, 100 °C and a maximum of 130 °C, based on the printer capabilities. The corresponding bulk crystallinity was measured using DSC and crystallinity weld microstructure was observed using AFM. Samples printed at 70 °C were annealed post-processing. The mechanical properties of all samples were tested through tear testing to determine the strength of individual welds and tensile testing for the properties of many layers.

Additional tensile sample geometries were printed at 70 °C and 130 °C to determine if crystallinity and corresponding mechanical properties could be duplicated for other print geometries. Two sample geometries were selected to create print layers that were parallel and perpendicular to tensile loading direction. The DSC crystallinity and tensile strength of these samples were measured.

Aim 3 – Investigate influence of printing processing conditions, post-process annealing, on monotonic tension and tensile fatigue of alternative high-performance thermoplastics (PEKK and PPSU)

While PEEK is one of the most common polymer for high strength orthopedic implants due to established high performance when injection molded or machined, other high performance thermoplastics could have better properties when 3D printed. PPSU is one potential thermoplastic in the high-performance classification that is amorphous making it more ideal for FFF printing. PEKK is a semicrystalline high-performance thermoplastic but with a slower crystallization rate than PEEK, also making it more ideal for FFF printing. PPSU and PEKK were printed at 70°C and 130°C build chamber temperature in two sample geometries to create print layers that were parallel and perpendicular to tensile loading direction. PEKK samples printed at 70°C were also annealed after printing. Further testing on PEKK included tensile fatigue.

2. Background

This section will review background information that informed the research objectives and gives context to experimental decisions and results.

2.1 Thermoplastics and Applications in Implantable Orthopedic Devices

2.1.1 What is a thermoplastic?

Thermoplastics are a polymeric class of materials that have a key quality of being able to be melted and reformed many times[1]. Most thermoplastics are linear or branched polymers with a flexible backbone chain. As these polymers are heated, the secondary bonding between chains decreases allowing for movement or flow of the polymer to the point of liquification when heated above the melt temperature. Thermoplastics will begin to irreversibly degrade if they are raised to too high of a temperature.

Thermoplastics can have either amorphous or crystalline structures. This crystallinity forms on a molecular level with ordered packing of the polymer chains. Due to the length and complexity of polymer chains, crystallinity is dispersed between amorphous regions resulting in semicrystalline materials. Polymers can have crystallinities ranging from totally amorphous up to about 95% crystalline with many semicrystalline polymers having maximum crystallinities much lower than 95%.

For semicrystalline polymers, crystallinity forms through melt crystallization when the polymer is cooled out of the melt or through cold crystallization (annealing) when the polymer is raised sufficiently above the glass transition temperature so that mobile polymer chains can pack into the crystalline structure. Crystallization is dependent on the structure of the polymer chain along with temperature and amount of time that polymers have to align into the crystalline structure. Amorphous polymers will never crystallize and will only go through a transition from rigid to soft at the glass transition temperature.

2.1.2 Mechanical behavior of thermoplastics

Thermoplastic mechanical behavior can be characterized through tensile stress-strain curves where materials are subject to uniaxial tension until failure. Key values including elastic modulus, yield strength and ultimate tensile strength. The elastic modulus is the relationship between stress and the deformation of the material in the region which the polymer can elastically recover. The yield strength is the stress at which the polymer begins to plastically deform, and the ultimate tensile strength is the highest stress value before the polymer fails. The specifics of stress-strain behavior depend on if a polymer is amorphous or semicrystalline. An amorphous polymer will deform elastically as chains elongate in the direction of the applied tensile stress. With continued applied stress, there is further elongation and alignment of the chains as they gradually move past each other and plastically deform until failure[1]. For a

semicrystalline polymer, the amorphous regions will initially elongate and elastically deform as previously described. With further applied stress there is also elastic deformation of the chains in the crystalline lamellae regions until a yield point is reached and the elongated chains begin to align until a yield point where stress will decrease as the polymer begins to neck. In the necking region, polymer chains begin to align increasing crystallinity and gradually increasing strength until ultimate failure.

The stress-strain behavior of a semicrystalline thermoplastic is also dependent on the amount of crystallinity[1]. A thermoplastic with increasing crystallinity will have higher strength, Figure 1. The tradeoff is that the ductility will decrease so as the crystallinity and strength increase, the polymer will not be able to deform as much and will fail at a lower strain.

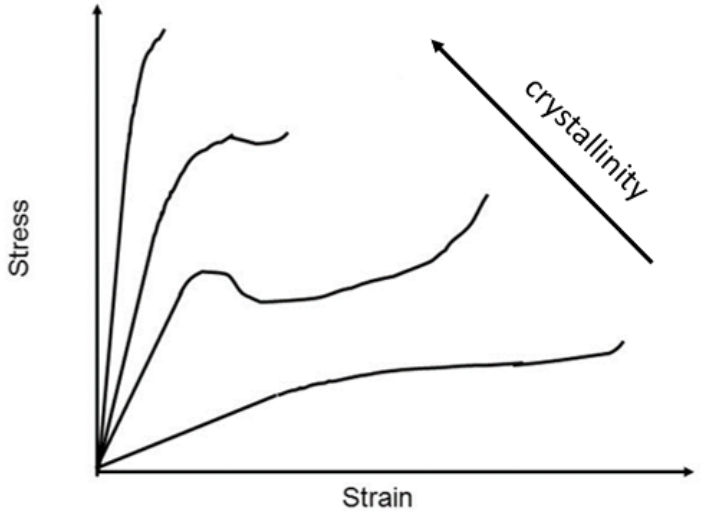

Figure 1: Chart depicting the stress-strain response of a semicrystalline thermoplastic with increasing crystallinity.

This research will explore other tests for quantifying the mechanical properties of 3D printed thermoplastics including tensile fatigue, compression testing and tear testing. Tensile fatigue is when a sample is subject to a cyclic tensile load until failure with key values of stress and cycles to failure. Compression testing is subjecting the sample to a uniaxial compression force instead of tension with similar key compressive properties including modulus and yield strength. Typically, polymers have higher strength in compression compared to tension. Tear testing is a measure of the materials resistance to propagation of tear through the material.

2.1.3 Applications of thermoplastics in orthopedic devices

Polyaryletherketones (PAEKs) are a class of high-performance thermoplastic polymers that are especially relevant in the medical field, particularly polyether ether ketone (PEEK). After its development in the 1990's, it began to replace metals in many applications due to its lower stiffness, radio-translucency, and higher strength compared to other polymers. Spinal disc surgery has had

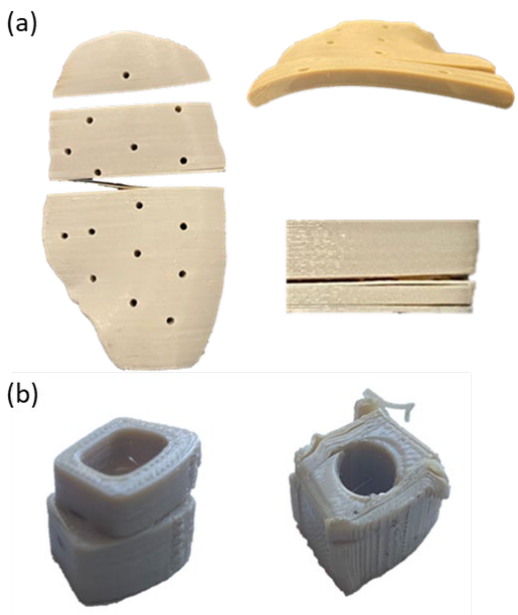

Figure 2: Layer delamination exhibited in 3D printed PEEK cranio implant (a) and torsion failure of PEEK spinal cage with different print orientations (b)

the largest adoption of PEEK devices, but PEEK's use has expanded farther to include craniomaxillofacial restoration, dental, suture anchors, pedicle shields, and spinal rods[2], [3]. 3D printing these polymers will create devices that can be complex for improved tissue integration, customized to patients' anatomy or provide quick iterations to improve the design and implementation process for medical devices. There has been some limited success producing PAEK medical devices using 3D printing, Figure 2. One report has 3D printed a cranio device using PEEK and implanted it in an animal study[4], but there are no companies producing devices using 3D printed PEEK. Oxford Performance Materials has developed 3D printed, patient specific polyether ketone ketone (PEKK) craniomaxillofacial devices and a spinal fusion cage[5]. However, craniomaxillofacial applications are non-load bearing and the mechanical property requirement is lower than most load bearing PAEK applications[2].

PAEKs are one of multiple types of thermoplastics used in 3D printing and medical device applications. Thermoplastics are common in implantable medical devices due to their mechanical properties and biocompatibility (there are cytotoxicity concerns with small molecules present in thermosets). Table I shows the classification of thermoplastic polymers, with selected thermoplastics that are common in medical devices and 3D printing bolded. Polylactic acid (PLA) is another semicrystalline especially of interest due to its wide use in the 3D printing. Polyphenylsulfone is an

amorphous thermoplastic, but is available for high performance medical applications, similar to PAEKs.

Table I. Classification of thermoplastic polymers with selected polymer in BOLD, list is not comprehensive

	Amorphous	**Crystalline**
High Performance	Polyetherimide, Polysulfones (PES, PSU, **PPSU**)	Polytetrafluoroethylene, Polyphenylene sulfide, **Polyaryletherketones (PEKK & PEEK)**
Engineering	Polycarbonate, Thermoplastic polyurethanes	Polyamides, Polyesters (PET, PCL, **PLA**)
Commodity	Polystyrene, Acrylonitrile butadiene styrene, Polyethylene terephthalate-glycol	Polyethylene, Polypropylene

2.2 3D Printing of Thermoplastics

2.2.1 3D printing methods for thermoplastics

The 3D printing methods for thermoplastics take advantage of their ability to be melted and reformed. The two main types of 3D printing for thermoplastics can be classified either as fused filament fabrication (FFF) or powder bed fusion (PBF)[6]–[8]. While there are some slight variations to these processes depending on the specifics the manufacturer of the printer, general overviews of the processes are described below.

Fused Filament Fabrication

This process is sometimes also referred to as material extrusion (ME) or fused deposition modeling (FDM). The starting material is in the form of an extruded polymer filament, normally a couple of millimeters in diameter. The printer includes a toolhead that can move in the xy plane and a build plate that can move up and down in the z plane. The toolhead consists of a motor to feed the filament, a hotend to melt the filament, and a nozzle for extruding the filament. The printer creates 3D objects by extruding the filament and moving the toolhead in the xy plane. After one layer is complete, the buildplate will move in the z direction to start a new layer. This continues until the 3D object is completed.

Powder Bed Fusion

The starting material for PBF is polymer powder. The printer includes a laser that sinters powder and moves in the xy plane, a build plate that moves in the z plane, a bed for unsintered powder and a roller to move powder from the fresh powder bed to the build plate. In this process, a single layer of unsintered powder will be rolled to the build plate. The laser will then raster over the layer to selectively sinter the polymer powder together. To form the next layer, the build plate will move down and a fresh layer of powder will be rolled over. This process of laser sintering and fresh powder layers will continue until the 3D object is complete. Afterwards, the unsintered powder will be removed to reveal the sintered polymer object.

While both these processes are compatible with thermoplastics, we chose to use FFF based on accessibility of the machines, low waste of raw materials, and control over printing parameters. FFF is a ubiquitous printing technology with the cost of machine ranging from hundreds to 10s of thousands of dollars. There are far fewer options for PBF (especially for high temperature polymers) and the cost ranges from 10s of thousands to 100s of thousands of dollars[9]. For some PBF materials, it is not possible to reuse unsintered powder from the bed so powder must be reprocessed before reuse, adding to the cost[10]. Commercially available PBF machines are often proprietary where the settings used are a black box specifically tuned to certain materials and the user has little control, making it more challenging to conduct a thorough research investigation into how the processing influences properties.

2.2.2 Key considerations for FFF printing and weld formation

The workflow of the FFF printing process, Figure 3, includes designing a 3D object and exporting it to an STL file format, importing the STL to a slicing software to select the parameters for printing and then exporting a g-code file from the slicing software that includes the instructions for the printer based on the STL geometry and the parameters selected in the slicing software. The parameters selected in the slicing software determine the toolpath and polymer extrusion during printing.

Figure 3: Work flow for 3D printing a computer-aided design (CAD) object

During the printing process, polymer is melted in the hotend and then extruded from the nozzle onto the previous layer (or build plate if it is the first layer). As it is extruded, the melted polymer and residual heat from nozzle heat the layer below. The polymer chains between the layers are mobile during the extrusion process so they relax and form a bond between the two layers, known as the weld. After extrusion, the layers cool and chain mobility stops when the material reaches a temperature below the glass transition temperature for the respective material. As processing is related to material properties, it is important to understand the impact of the printing parameters, specifically how they influence the weld formation between printed fibers.

2.3 Mechanical Behavior of FFF Thermoplastics

2.3.1 Print parameters impact on mechanical properties

One approach to understanding the impact of processing on the properties of 3D printed materials is to vary the printing parameters and measure the corresponding mechanical properties. Key processing parameters that can be modified in the slicing

software include layer height, extrusion width, print speed, nozzle temperature, build chamber temperature, perimeter number, infill percent and print orientations of the build.

There have been many research papers that investigate how these printing parameters influence the mechanical properties of FFF processed thermoplastics, including PLA and PEEK, but limited conclusive results due to variability between printers, number of parameters that can be adjusted (and the dependence of those parameters on each other), and non-standardized sample geometries and testing procedures[11]. Many of these papers use design of experiments and optimization techniques to maximize tensile strength. Process parameters that result in best mechanical properties include high nozzle temperature, low layer height, and maximum infill/overlap of fibers[12], [13], but varying printing conditions are used as there are no testing standards for FFF materials, as mentioned previously. Some ASTM and ISO standards are acceptable for use with FFF materials but they are either limited in their applicability or must be modified for use on FFF materials[11]. The existing standards do not address the additional complexity of 3D printing processing variables and difficulty of creating test structures (dogbones are not a "printer friendly" structure).

Additionally, there are few investigations relating FFF process parameters to weld formation and the structure of the material. Initial studies show that FFF processing conditions influence weld formation factors:

1. Coalescence of fibers (polymer chain diffusion across weld)[14]
2. Thermal stresses[15]
3. Porosity[16]
4. Morphology and crystallinity[17] (for semicrystalline thermoplastics)

While process parameters impact the mechanical properties, it is important to relate the processing-property relationship to the above weld factors to deepen the understanding of properties and create repeatable results.

2.3.2 Weld formation impact on mechanical properties

One key reason the parameters impact the mechanical properties of printed parts is due to how they effect the weld formation between layers, Figure 4. To address the mechanical anisotropy of FFF thermoplastics, it is necessary to understand the processing-structure relationship at the weld. Current research explores the requirements for weld formation in amorphous polymers which finds that polymer chains need to be held at a temperature above T_g for a sufficient amount of time for the polymer chains to diffuse[14], [18] and there needs to be adequate contact between the printed layer and the layer below it[19]. Semi-crystalline polymers have the additional phenomena of crystallization while printing[20]. Specifically, it has been demonstrated that crystallinity can improve strength if cocrystallization occurs across welds. If cocrystallization across the weld does not occur, materials are weaker[20].

Investigations of FFF PLA (most investigated FFF semicrystalline thermoplastic) have used changes in the build plate temperature or annealing to increase crystallinity and investigate impact on mechanical properties. The crystallinity was measured using differential scanning calorimetry, x-ray spectroscopy and observed using polarized optical light microscopy (POM) and/or scanning electron microscopy (SEM). While increased crystallinity contributed to an increase in stiffness[21], flexural strength[22] and impact strength[20], these studies did not address the anisotropic nature of FFF PLA and they did not investigate cocrystallization across the weld. McIlroy, et al. used modeling to show increased crystallization at the weld due to flow crystallization during printing. They suggested that this increased crystallinity could improve the weld strength but no experimental mechanical testing was provided to support that hypothesis[17]. Additionally, other studies show that once crystallization begins during printing, fiber coalescence stops. Cold crystallization annealing can happen during printing with subsequent layer deposition [23], further

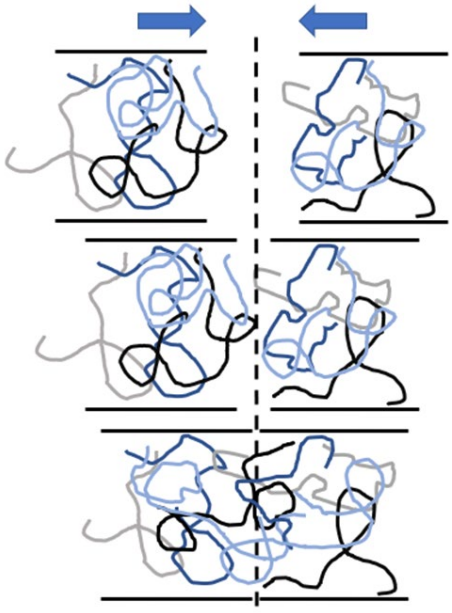

Figure 4: Weld formation process of an amorphous polymer through interdiffusion of polymer chains

inhibiting polymer chain diffusion. Investigation is needed to understand the relationship between crystallization and polymer chain diffusion from the glass transition temperature to the melt temperature.

2.3.3 Annealing impact on mechanical properties

For semicrystalline thermoplastics, annealing can be used to increase crystallinity and, therefore, increase strength, as shown in Section 2.1.2 Figure 1. However, it is unclear if this relationship applies to FFF materials. In 3D printing "welding" literature, co-crystallization across an interface is necessary to increase strength [20], [24], Figure 5a, which is not guaranteed with annealing. When crystallinity forms without co-crystallization, there is a weakening of properties [24], Figure 5b.

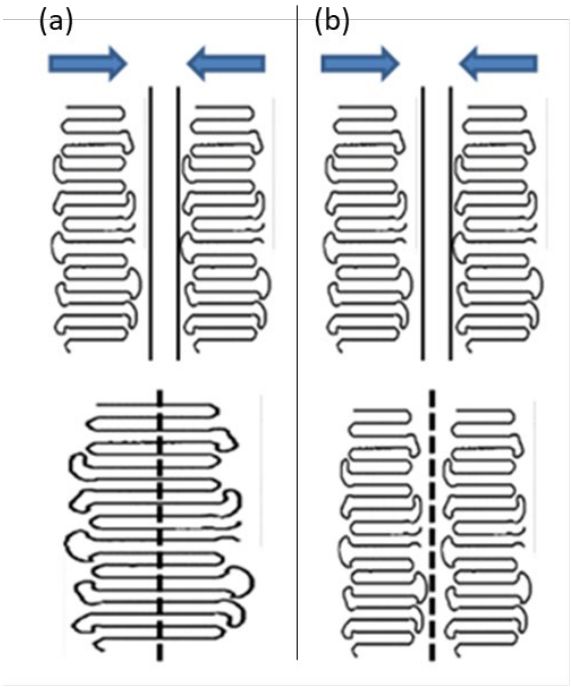

Figure 5: Schematic depicting co-crystallization that forms at the weld (a) and crystallization inhibiting chain interdiffusion across the weld (b)

Current literature hypothesizes that annealing improves the properties of FFF PLA through increasing crystallinity at or across the weld [17]. However, there is limited mechanical testing data in the literature that supports this hypothesis, and it is unclear

how annealing influences other factors including thermal stresses at the weld and porosity. Some studies have explored annealing of FFF PLA and PEEK but have shown little improvement in mechanical properties and most of them do not address the effect of fiber orientation and weld weakness [25], [26], [27] [28] [21]. Only one study showed that annealing increases crystallinity and tensile strength[29], but they did not observe the morphology of the crystallinity or address anisotropy.

Additionally, once crystallization begins during printing, fiber coalescence stops. Cold crystallization annealing can happen during printing with subsequent layer deposition [23], which may pose challenge to annealing materials to improve weld strength if crystallization that formed during printing inhibits the required molecular mobility . So, while crystallinity may be increasing during the annealing of FFF materials, there has not been an investigation into whether spherulites are co-crystallizing across the interface of FFF welds.

3. Effect of print processing and post-process annealing on PLA mechanical properties

3.1 Introduction

Polylactic acid (PLA) has emerged as a popular filament for fused filament fabrication (FFF) 3D printing due to its low melting temperature and reliable print morphologies. Due to the layer by layer extrusion nature of FFF, printed parts have anisotropic mechanical behavior due to inherent weaknesses at the weld between fiber layers. This is true for all materials printed with FFF, including PLA. Tensile properties often closely match injection molded properties when printed fibers are oriented in the testing direction, but when printed fibers are oriented perpendicular to the testing direction there is a significant reduction in mechanical properties [25]. FFF parts can be designed to accommodate anisotropy by orienting fibers in the direction most suitable for loading but many applications have complex loading profiles that will challenge weaknesses across the fiber-to-fiber weld present in subsequent layers.

It is well documented that printing parameters affect mechanical properties [31]–[35] but it is still unclear how the underlying structural factors that affect mechanical properties are influenced by printing parameters. This lack of understanding makes it difficult to select printing parameters to achieve optimal mechanical properties. Initial studies have shown that FFF processing conditions influence the coalescence of fibers (polymer chain diffusion across weld) [36], thermal stresses [15], [37], porosity [16], morphology and crystallinity [17]. However, there is limited exploration of these

factors' work in conjunction to dictate mechanical properties and how they can be leveraged to improve mechanical properties, either during printing or with thermal post-processing.

Annealing is a post-processing method that is hypothesized to improve the mechanical properties of FFF PLA, as it does for injection molded PLA [38]. One hypothesis is that annealing improves the properties of FFF PLA through increasing crystallinity at or across the weld [17]. However, there is limited mechanical testing data in the literature that supports this hypothesis, and it is unclear how annealing influences other factors including thermal stresses at the weld and porosity. Some studies have explored annealing of FFF PLA but have shown little improvement in mechanical properties and most of them do not address the effect of fiber orientation and weld weakness [25]; [27] [28] [21]. When examining the impact of thermal annealing on changes in crystallinity and porosity, it is essential to consider loading modes with tensile stresses both parallel and perpendicular to the interfacial weld normal. Loading in tension perpendicular to the interfacial weld normal is a direct measure of weld strength while loading parallel to the weld normal assesses the materials inherent strength in the essential absence of a weak weld region.

While it is typical for an increase in crystallinity to increase the basic strength of injection molded PLA, these studies fail to consider weld behavior innate to FFF PLA. In 3D printing "welding" literature, co-crystallization across an interface is necessary to

increase strength [20], [24]. When crystallinity forms without co-crystallization, there is a weakening of properties [24]. Additionally, once crystallization begins during printing, fiber coalescence stops. Cold crystallization annealing can happen during printing with subsequent layer deposition [23]. So, while crystallinity may be increasing during the annealing of FFF PLA, there has not been an investigation into whether spherulites are co-crystallizing across the interface of FFF welds. The hypothesis that annealing will improve mechanical properties of FFF PLA does not account for weaknesses at the weld due to crystallinity limiting polymer chain diffusion during printing and inhibiting co-crystallization during annealing.

The goal of this study is to understand how annealing impacts porosity, crystallinity and weld morphology to determine how those factors affect tensile strength depending on the orientation of printed fibers. This is done using two experimental approaches and comparing samples with a flat print orientation to samples with an upright print orientation. The first experiment investigates a scan of printing parameters and annealing times and temperatures above the cold crystallization temperature (T_{cc}) for PLA. The second experiment investigates annealing above and below T_{cc} at multiple points over 12 hours. This work was done in collaboration with David Collinson who collected the AFM images and Trent Lau who contributed to the MicroCT porosity data analysis.

3.2 Materials and Methods

3.2.1 PLA FFF Processing

PLA (MatterHackers – PLA Pro filament) dogbones (D638 Type V, 1.5 mm thickness) for tensile testing were sliced using Ultimaker Cura and printed using an Ultimaker 3. PLA filament was placed in a drying oven for at least 6 hrs at 50°C before printing to remove moisture. Based on previous research, dogbones were printed in best- and worst-case print orientation and raster pattern [39]. Best-case dogbones were printed flat in the XY plane with fibers oriented parallel to testing direction, Figure 6A, and worst-case dogbones were printed upright in the YZ plane with fibers oriented perpendicular to testing direction, Figure 6B.

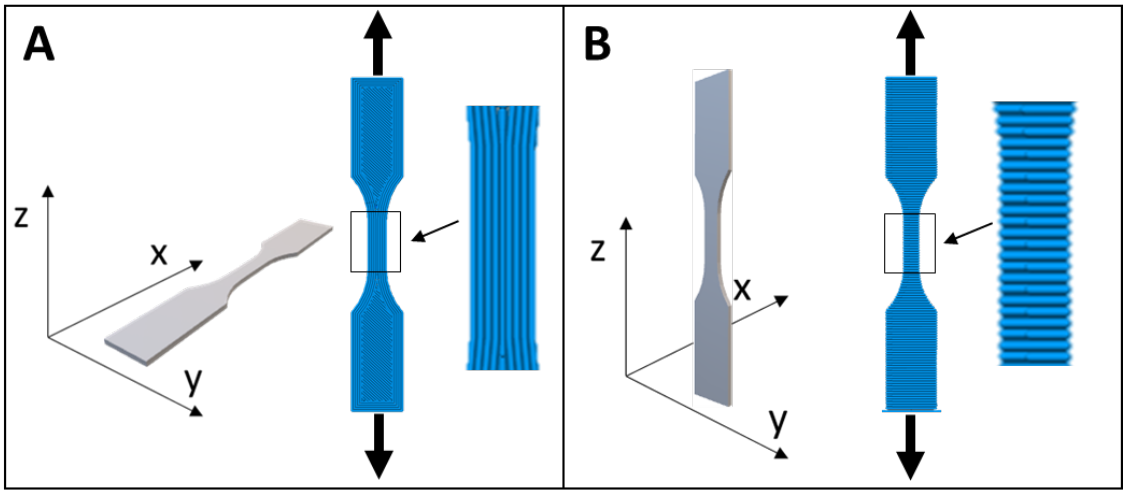

Figure 6: Print orientation and tensile testing direction for XY (A) and YZ (B) samples.

Layer height and print speed parameters were varied by selecting a low and high value – 0.1 mm and 0.3 mm for layer height, 20 mm/s and 60 mm/s for print speed, Table

II. All other print parameters were kept constant, some key parameters include a 205°C nozzle temperature, 60°C build plate, and a 0.4 mm nozzle diameter.

Table II: A-D print parameters

Print Parameters	Layer Height	Print Speed
A	0.1 mm	60 mm/s
B	0.1 mm	20 mm/s
C	0.3 mm	60 mm/s
D	0.3 mm	20 mm/s

3.2.2 Annealing of printed dogbones

After printing, dogbones were either tested as printed or annealed before testing. Flat and YZ dogbones with print parameters A through D (Table) were annealed at 80°C and 95°C for 15 minutes and 1 hour. XY and YZ dogbones with print parameters B were additionally annealed at either 65°C (below T_{cc}) or 80°C (above T_{cc}) for 15 minutes, 1 hour, 3 hours, 6 hours, or 12 hours. The glass transition temperature (T_g) of the PLA filament is 59.5°C, as measured with differential scanning calorimetry (DSC). A heating rate of 20°C/min and the second heat pass of a heat – cool – heat cycle was used to determine T_g. The anneal temperatures of 65°C and 80°C were determined to be below/above T_{cc} through experimentally annealing samples and measuring crystallinity with DSC.

3.2.3 X-ray Computed Tomography (MicroCT) analysis

The porosity of printed dogbones was quantified using MicroCT (Nikon XTH 225 ST) and Avizo software. Dogbones were scanned with a voxel size of 10.85 μm, 125 Kv beam energy, 9.8 W, and a 78 μA current. This resolution detects airgap porosity between printed fibers but it is not fine enough to measure porosity within printed fibers. To analyze the airgap porosity, a subsection of the gauge section of each dogbone was selected. This subsection was thresholded to distinguish the solid and airgap fractions. The porosity reported is the airgap fraction of the total volume of the selected subsection.

3.2.4 Differential Scanning Calorimetry (DSC) analysis

The crystallinity of the filament, as printed, and annealed was determined using DSC (TA Discovery 2500). Approximately 10mg was cut from dogbone samples and heated at 10°C/min in a nitrogen environment. The percent crystallinity was determined from the first pass ΔH_m divided by the theoretical ΔH_m of 93.64 J/g for 100% crystalline PLA [40].

3.2.5 Monotonic tensile testing

The stress-strain behavior of the printed dogbones was determined through monotonic tensile testing (Test Resources 830EL63). Dogbones were tested at a displacement rate of 1 mm/min until failure. Failure is defined as the fracture of one or all of the printed fibers in the sample resulting in a decrease in stress. The cross-section

dimensions of samples were measured with calipers before testing. Strain was measured by marking tracking points on the sample before testing and using a video extensometer system.

3.2.6 Atomic Force Microscopy

Atomic force microscopy (AFM) scans were collected across the weld region between fibers of select samples, Figure 7B, to observe polymer structure and crystallinity at the interface between fibers. To prepare samples for AFM, sections were cut from dog bones using a diamond saw, Figure 7A, and then a surface for AFM analysis that included the weld interface (Figure 7B) between two fibers was wet-sectioned at room temperature using a UC7 Ultramicrotome (Leica, Germany) to produce a smooth surface, with a roughness of R_a = 0.83 nm as measured by AFM in the amorphous regions of the samples. The cutting direction during sectioning was perpendicular to the weld interface to preserve the weld structure.

AFM images were acquired in tapping mode using a Cypher ES (Asylum Research, USA) atomic force microscope (AFM) (Asylum Cypher Atomic Force Microscope) across the weld region of select samples, Figure 7B, to observe the change in morphology of crystalline domains, if any, at the weld interface. Measurements were acquired at room temperature with a silicon cantilever (AC160, Olympus) with a nominal tip radius of 7 nm that was driven on resonance using BlueDrive(TM). The resonant frequency, cantilever stiffness and quality factor of the fundamental cantilever mode was 70.8 kHz,

2.9 N/m, and 176 respectively. For scanning, the cantilever was excited using the 3rd cantilever eigenmode, which had a resonant frequency, cantilever stiffness and quality factor of 1.1 MHz, 293 N/m, and 683.44 respectively. The 3rd eigenmode is used as the high effective stiffness and quality factor enables stable and fast scanning over the rough crystalline domains while maintaining low forces due to the small oscillation amplitudes used, with a typical free air amplitude of 14 nm and setpoint of 10 nm.

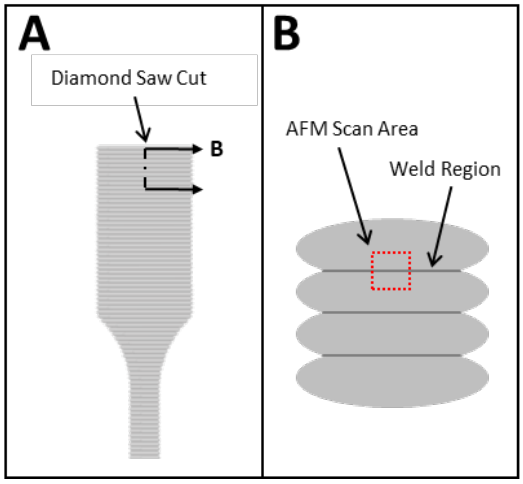

Figure 7: Schematic of diamond saw cut location on dogbone (A) and cross section from dogbone cut including weld region imaged with AFM (B).

3.3 Results

The following sections include the results for the two experiments. The first experiment investigates a scan of printing parameters and annealing times and temperatures above T_{cc}. Print quality and crystallinity of these samples is determined

using MicroCT and DSC, respectively. Tensile testing determines how print quality and crystallinity impact mechanical properties of the samples. The second experiment investigates annealing above and below T_{cc} at multiple points over 12 hours. Porosity and crystallinity are quantified using MicroCT and DSC, respectively. Tensile testing determines how the porosity and crystallinity impact mechanical properties. Finally, AFM is used on select samples to observe polymer morphology and crystallinity in the weld region.

3.3.1 Scan of printing parameters and annealing

The following section presents the results for the first experiment investigating a scan of printing parameters and annealing times and temperatures above T_{cc}.

3.3.1.1 MicroCT print quality

MicroCT scans show the print quality (porosity and "macroscopic" connectivity of fibers in dogbones) for all printing conditions, Figure 8. These qualitative images show how the pores in 0.1 mm layer height dogbones are smaller and more numerous while there are fewer, but larger pores in 0.3 mm layer height dogbones. Connected adjacent pores are the same color while disconnected adjacent pores are different colors. Dogbones printed with the faster speed have larger pores that are more likely to be connected, meaning there is a poorer connection between the printed fibers. Additionally, the print orientation dictates the directionality of the pores. For XY

samples, pores are parallel to the loading direction for tensile testing and they are perpendicular to the loading direction for the YZ samples.

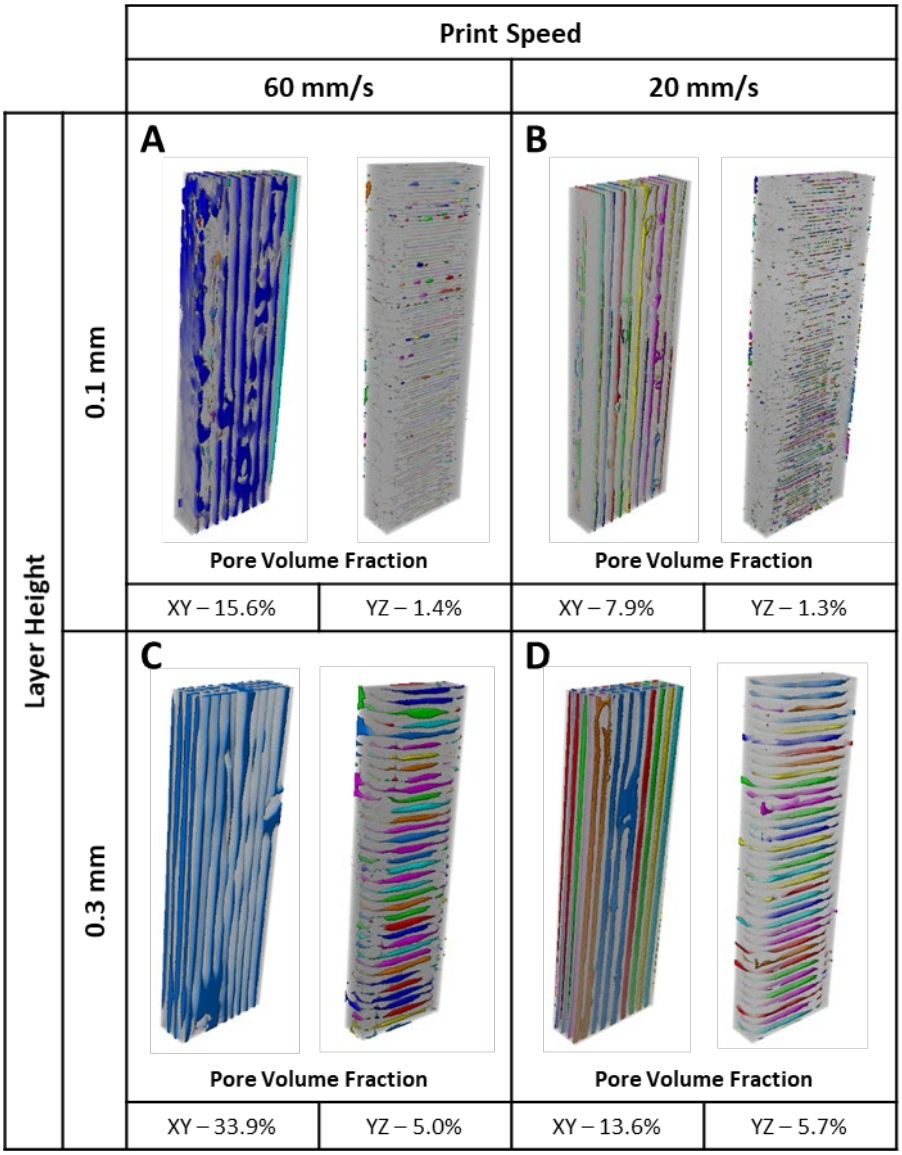

Figure 8: Avizo images of porosity analysis on dogbone gauge subsection for print parameters (A-D) , colors represent connectivity of adjacent pores. Percent porosity based on airgap volume fraction is listed below each image.

3.3.1.2 Differential Scanning Calorimetry

DSC of as provided and annealed PLA filament shows how crystallinity increased with temperature and time, Table III. Filament annealed at 80°C for 15 minutes had a slightly higher average crystallinity (4.9%) compared to the filament as provided (4.1%). Increasing the time and temperature increased the crystallinity with annealing at 95°C for 60 minutes achieving a crystallinity of 23.3%.

Table III: Crystallinity of as provided and annealed PLA filament, n = 3.

Annealing Temperature (°C)	Annealing Time (minutes)	ΔH (J/g) Average ± STD	Crystallinity (%)
As provided	As provided	1.71 ± 0.55	1.8 %
80	15	3.83 ± 0.34	4.1 %
80	60	10.91 ± 1.1	11.7 %
95	15	20.47 ± 0.65	21.9 %
95	60	40.87 ± 0.43	43.6 %

3.3.1.3 Tensile strength

The ultimate tensile strength (UTS) of FFF PLA dogbones was highly dependent on print orientation, Figure 9. The XY samples resulted in a maximum UTS of 53.9 MPa (Figure 9B- low layer height, low print speed) and minimum UTS of 41.9 MPa (Figure 9C - high layer height, high print speed) while the YZ samples resulted in a maximum UTS of 33.8 MPa (Figure 9A – low layer height, high print speed) and minimum UTS of 20.1 MPa (Figure 9C – high layer height, high print speed). There was only a 23%

reduction in UTS from XY to YZ samples for A print parameters while in the worst case (D print parameters) there was a 55% reduction.

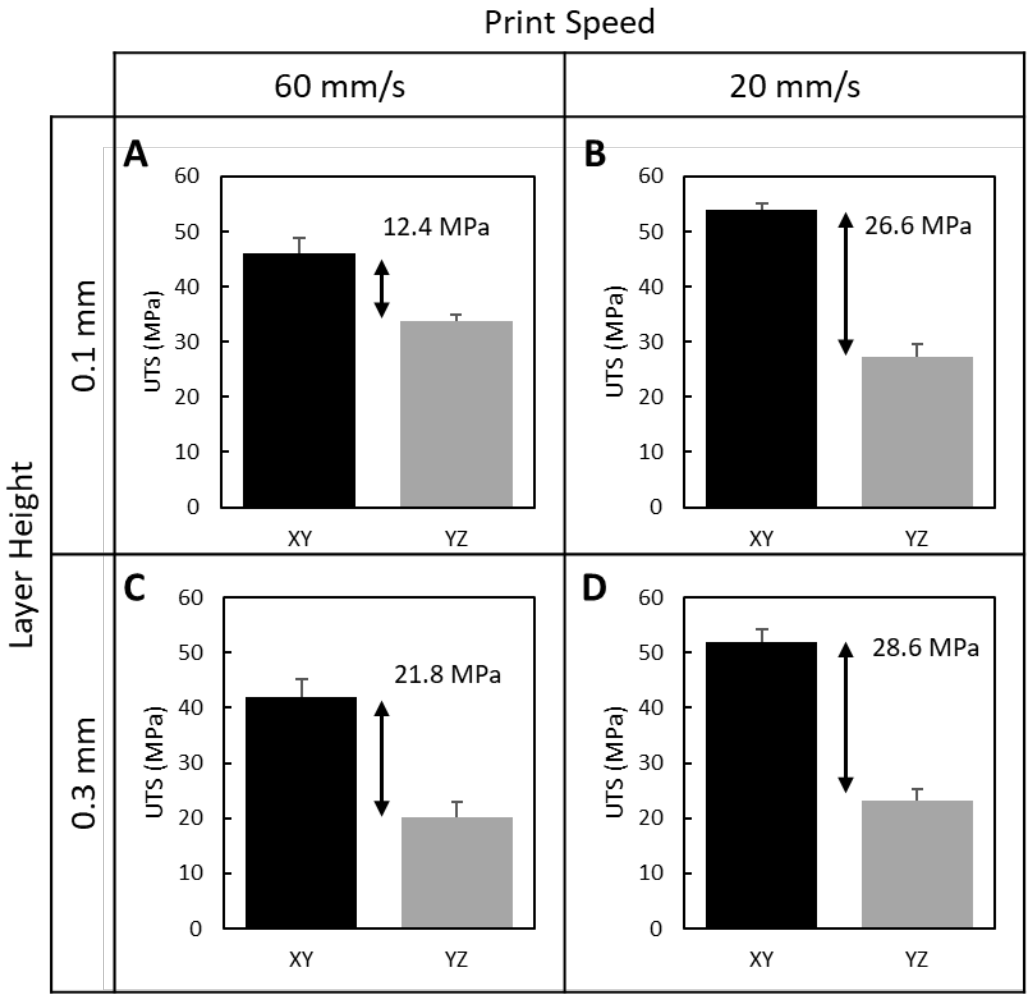

Figure 9: Ultimate tensile strength (UTS) for XY and YZ samples with scanned printing parameters A-D. The arrow indicates the difference between mean UTS for samples. Error bars represent one standard deviation, n = 4.

Annealed dogbones were also tested to see if an increase in crystallinity increased UTS. For the XY samples, annealing resulted in either no change or a decrease ($p < 0.05$) in UTS for all print parameters and annealing conditions, Figure 10. Annealing

conditions with higher crystallinity resulted in decreased UTS. For the C – XY printing conditions, the drastic decrease in UTS of the samples annealed at 80°C for 60 minutes and the samples annealed at 95°C for 60 minutes falls outside the trend of the other samples. This is likely due to variability during printing such as build plate levelness or material building up in the nozzle and inadvertently decreasing extrusion. Samples printed with the C print parameters are of poorer quality and more susceptible to a negative impact due to print variability.

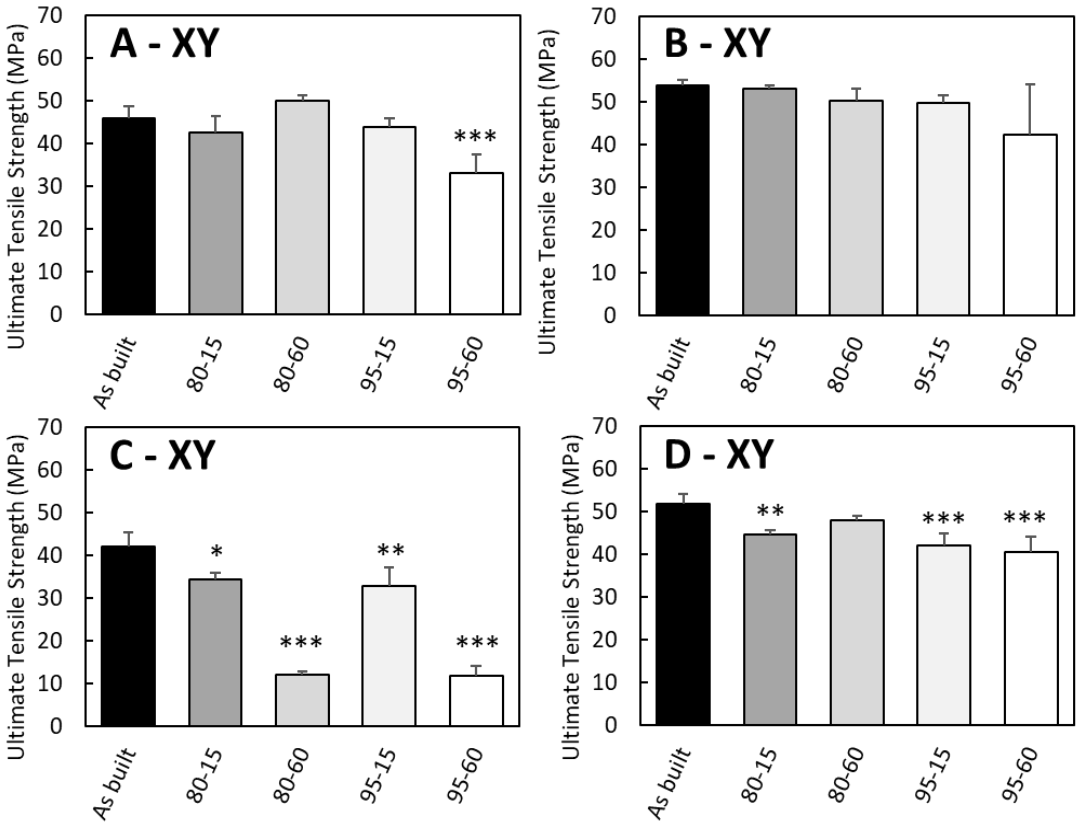

Figure 10: Ultimate tensile strength for XY samples (A-D print parameters) with scanned annealing parameters. One-way ANOVA with T-test was used to determine significance of annealing compared to the as built treatment, *p<0.05, **p<0.01 ***p<0.001. Error bars represent one standard deviation, n = 4.

A similar trend was observed in the YZ samples, Figure 11. There was no significant increase in strength with annealing and some annealing conditions resulted in decrease in strength ($p<0.05$). For the D – YZ printing conditions, the decrease in UTS for the samples annealed at 80°C for 60 minutes and the samples annealed at 95°C for 60 minutes falls outside the trend of the other samples. As with the C – XY samples, this is likely due to variability during printing.

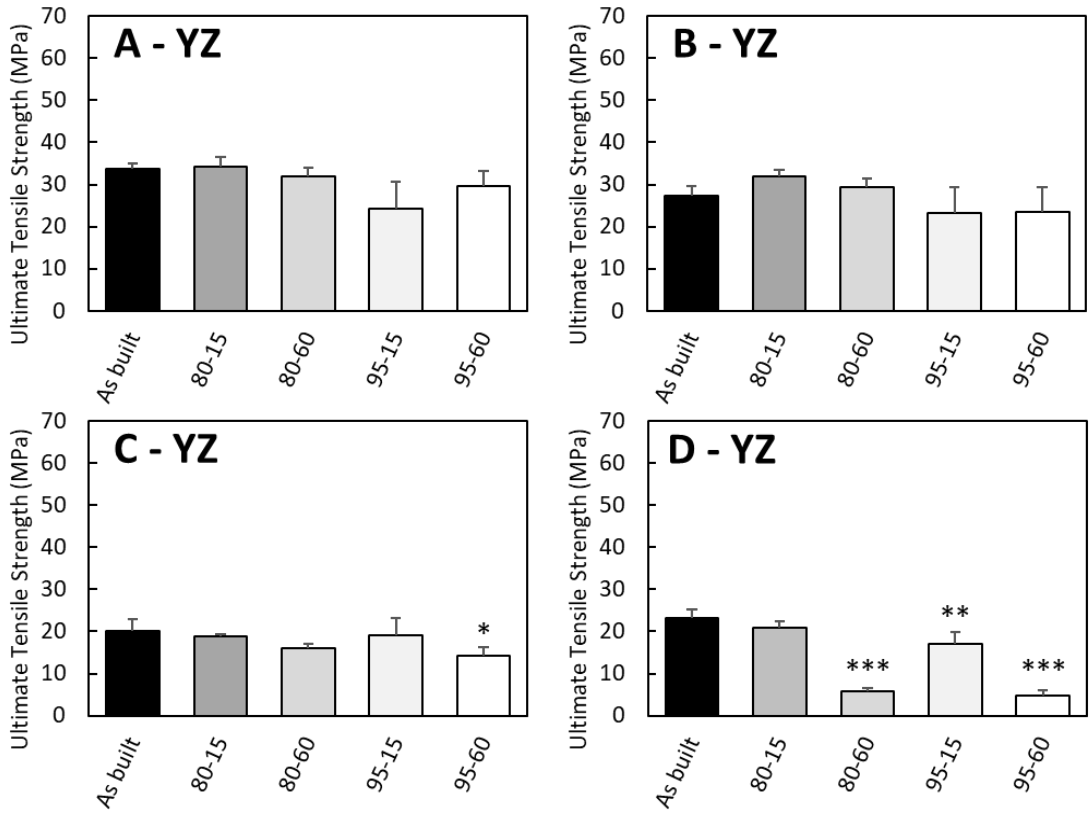

Figure 11: Ultimate tensile strength for YZ samples (A-D print parameters) with scanned annealing parameters. One-way ANOVA with T-test was used to determine significance of annealing compared to the as built treatment, *p<0.05, **p<0.01 ***p<0.001. Error bars represent one standard deviation, n = 4.

3.3.2 Annealing above and below cold crystallization

The following section presents the results for the second experiment investigating annealing above and below T_{cc} at multiple points over 12 hours. For this section, only dogbones printed with B printing parameters (low layer height, low print speed) were tested given these parameters resulted in the best samples and mechanical properties across YZ and XY samples and with multiple printing efforts.

3.3.2.1 Porosity

The porosity, as measured and analyzed using MicroCT, of the B print parameter dogbones is plotted against annealing time and temperature for both the XY and YZ samples, Figure 12. There is no clear trend between porosity and the annealing time/temperature. On average, XY dogbones had a higher porosity than YZ dogbones.

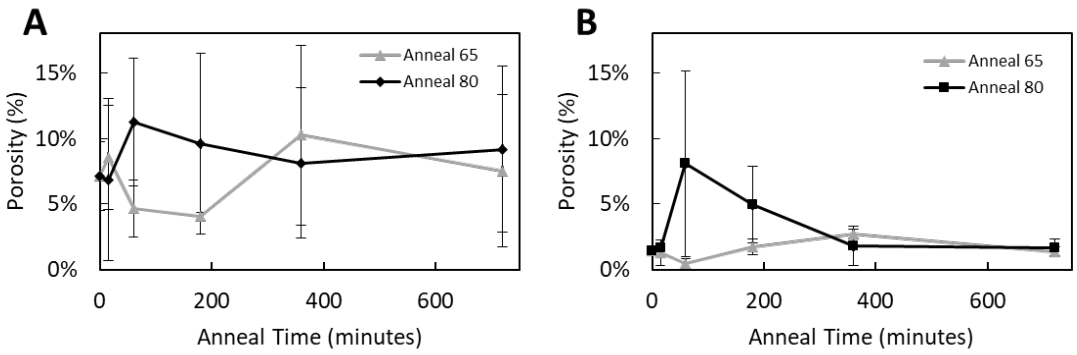

Figure 12: Percent porosity for XY (A) and YZ (B) samples over anneal time. Error bars represent one standard deviation, n = 3.

3.3.2.2 Crystallinity

XY and YZ oriented dogbones with B print parameters were annealed above T_{cc} (80°C) and below T_{cc} (65°C) for up to 12 hours, Figure 13. While samples annealed above T_{cc} increased in crystallinity up to approximately 33% crystallinity for samples annealed for 12 hours, samples annealed below crystallization did not significantly increase in crystallinity.

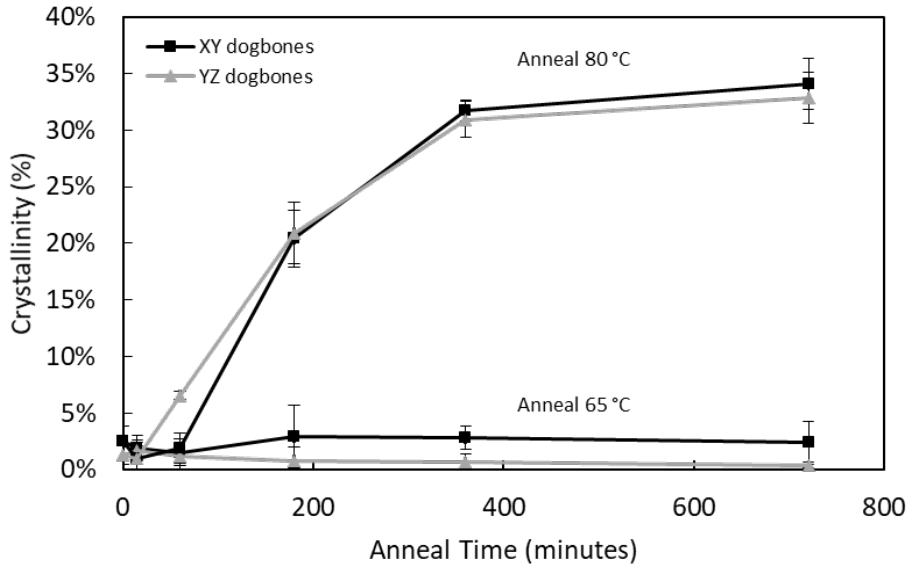

Figure 13: Crystallinity percentage for XY and YZ samples as a function of anneal time. Error bars represent one standard deviation, n = 3.

3.3.2.3 Tensile strength

As observed under previous conditions, the UTS of PLA with these annealing conditions was highly dependent on print orientation (all samples tested had B print parameters), Figure 14. While there was no increase in UTS for samples annealed above

T_{cc} at 80°C, there was an increase for samples annealed below T_{cc} at 65°C. A maximum UTS of 64 MPa was achieved for the XY samples and a maximum UTS of 37 MPa was achieved for the YZ samples, both with annealing at 65°C for 6 hours.

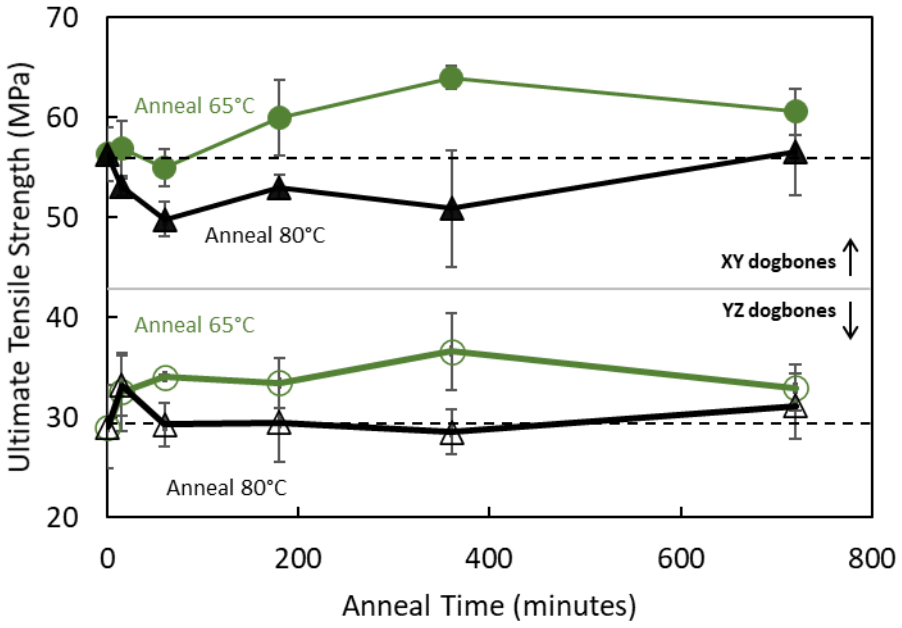

Figure 14: Ultimate tensile strength as a function of anneal time. Error bars represent one standard deviation, n = 4. Dashed lines represent baseline tensile strength of as printed samples.

The UTS data was plotted with crystallinity and porosity to determine the overall relationship between the structure and tensile properties, Figure 15. While crystallinity increased, there is not an increase in UTS. Likewise, samples with improved UTS do not show an increase in crystallinity. There is also no clear relationship between porosity

and UTS. The porosity of the YZ samples is lower than the XY samples; however, the UTS of the YZ samples is also lower.

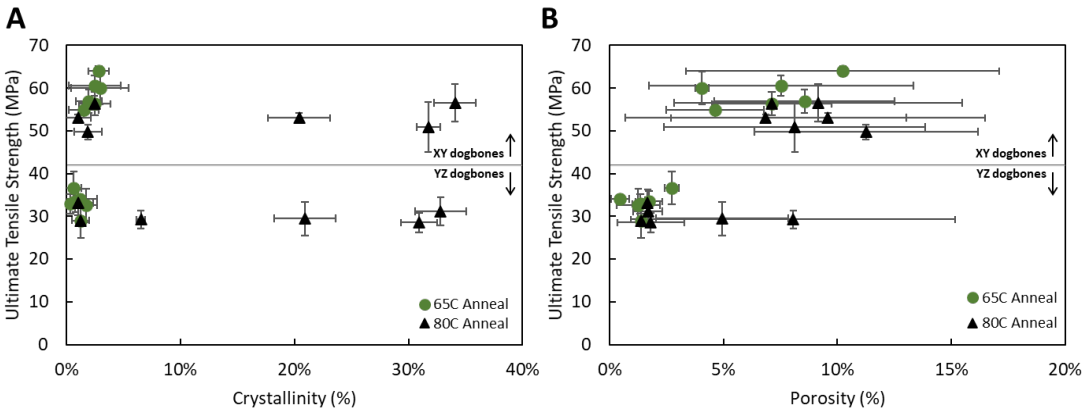

Figure 15: Ultimate tensile strength as a function of percent crystallinity (A) and porosity (B). Error bars represent one standard deviation.

3.3.3 Atomic force microscopy (AFM) of as printed and annealed PLA weld regions

AFM images of select YZ samples demonstrate how the interface at the weld region between filaments exhibits different morphology than the bulk of the fiber filaments as well as the evolution of the PLA with annealing, Figure 16 and a larger scale in Figure A1. For the as printed sample, Figure 16A, there appears to be distortion at the interface with low crystallinity, possibly due to incomplete welding during printing. Subsequent annealing of the dog bones reduces the distortion of the interface as the PLA relaxes. For the sample annealed at 65°C for 12 hrs, the interfacial layer completely "heals", and no discernable interface could be observed in AFM, Figure 16D. For the samples annealed at 80°C, a partially healed interfacial layer can still be observed after

15 min of annealing along with the nucleation and growth of spherulites preferentially on or near the weld interface, Figure 16B. Comparatively, few spherulites are observed in the bulk of the 85°C-15 min sample. For the sample annealed at 80°C for 12 hours, Figure 16C, spherulites pervade the entire sample, but the interface in the weld region is still observed as spherulites near the weld interface do not bridge the interface between the welds and a change in local crystalline structure can be observed.

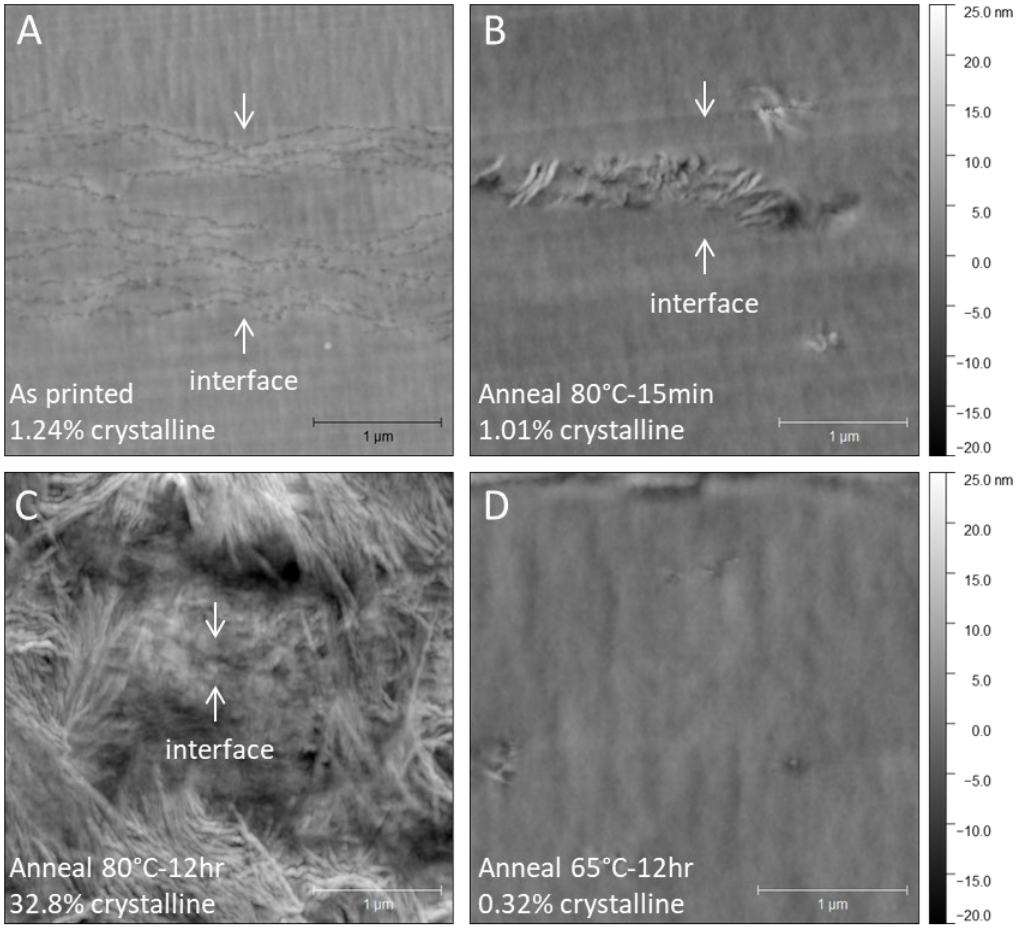

Figure 16: AFM images of weld regions for as printed (A), 80°C-15 minute anneal (B), 80°C-12 hour anneal (C), and 65°C-12 hour anneal (D) samples with DSC average crystallinity values. Each scan is 3.5×3.5 µm and consists of 512×512 pixels collected at a scan rate of 0.5 Hz. The crystalline domains in the sample are observed as feature into the height due to preferential fracture along crystallographic planes during microtoming leading to high surface roughness and distinct structure compared to the amorphous polymer.

3.4 Discussion

Previous PLA FFF studies have explored how printing parameters influence tensile properties. Consistent with those studies, we found that the print orientation and the direction of the printed fibers relative to tensile testing direction had the largest

impact on tensile strength [12]. While print "quality" (measured by porosity) varied based on print parameters (layer height changes the shape and connectivity of the printed fiber and print speed impacts weld development during printing [41]), the print orientation played a far larger role in tensile strength, Figure 9. These results indicate the inherent interfacial weld strength plays a far greater role than measurable porosity or crystallinity at (but not across) the interface.

Annealing of PLA has been hypothesized as a way to increase the mechanical properties of printed PLA through increasing crystallinity [17]. However, our data shows that while annealing increases the crystallinity of the sample, tensile strength does not increase and in some cases it decreases as a result of annealing, Figure 10 and Figure 11. This finding suggests that the polymer chains do not co-crystallize across the interface boundaries in the weld, and crystallinity is in fact detrimental to the strength of the dogbone under these print and annealing conditions. Instead, the interfaces between fibers become more brittle and flaw intolerant as crystallinity increases. While it might be expected that samples with fibers oriented in the direction of testing (XY samples) would improve as the welds are parallel to the testing direction, our data still shows there is either a decrease in strength or no improvement. Even though the fibers are oriented in the testing direction, the weak interfaces between those fibers could possibly create flaws that contribute to early failure. Additionally, as the samples crystallize

during annealing, there is also a volume change that results in some sample warping that could also contribute negatively to tensile strength.

Our exploration of time-mediated annealing above (80°C) and below (65°C) T_{cc} further investigates the relationship between annealing and improving tensile strength by addressing porosity, crystallinity, and weld morphology. While porosity is a factor that impacts the mechanical properties of FFF PLA [21], we did not observe a significant change in porosity through annealing at these conditions, Figure 12. The porosity of YZ printed samples was significantly lower than the XY samples but the directionality of the porosity dominated. Porosity in the XY samples was parallel with the printed fibers and the testing direction while porosity in the YZ samples was between fibers and perpendicular to testing direction. In comparing these two situations, the porosity across the fibers is likely more detrimental when it is in a plane normal to the tensile loading direction. However, with an inherently weak interface, the porosity (even in the plane of tensile loading in the YZ samples) is likely not the largest contributor to material weakness and removing the porosity completely may not result in high strength.

Annealing above T_{cc} increases crystallinity, Figure 13, and influences weld morphology, Figure 16. Previous studies show that chain alignment induced during printing increases the crystallization rate near the interface between filaments during annealing [17], leading to spherulites preferentially forming near the weld, as shown in

Figure 11B. This crystallinity limits chain mobility during printing, inhibiting diffusion across the interface and subsequent annealing above T_{cc} then further increases the crystallinity of the samples preventing complete healing of the as-printed weld. While crystallinity could increase the strength of interfaces, the polymer chains need to co-crystallize across the interface, which does not occur in this study. A discontinuous junction promotes brittle fracture. This is also supported by the AFM data where the interface between fibers is still visible even with long annealing times which result in crystallinity pervading the entire sample, Figure 16C.

Annealing below T_{cc} heals the weld without increasing crystallinity, Figure 13. The T_{cc} is above the glass transition temperature so polymer chains are mobile but crystallinity does not increase because spherulite growth is inhibited. The limited mobility of the polymer chains in this temperature range between glass transition and T_{cc} enables weld healing without increasing crystallinity. When samples were annealed below T_{cc} but above T_g (at 65°C) there was an increase in UTS with annealing time, Figure 14. The AFM data shows incomplete weld formation at the interface in the as-printed sample but with annealing at at 65°C the weld is no longer visible, Figure 16D. This suggests that there could be some "healing" of the interface driven by the annealing relaxing the polymer material and improving cohesion between the fibers.

If annealing that induces crystallinity is used as a post processing strategy, chain diffusion across the fiber interfaces must be facilitated so that the as-printed weld

interface, Figure 16A, can first completely heal followed by co-crystallization across the interface. As such, initial annealing of PLA below T_{cc} followed by subsequent annealing above T_{cc} to induce crystallization may be the best approach for optimizing the properties of PLA, but further studies are needed to better understand how crystallinity forms during printing and its role in polymer chain diffusion during interface formation. While it is hopeful that annealing will increase strength with appropriate protocols, it is necessary that the fibers are sufficiently welded so that co-crystallization between fibers occurs, otherwise increasing crystallinity through annealing can result in weaker welds and a decrease in strength.

Further studies need to be conducted on the formation of the weld to improve weld strength and reduce anisotropy, including the relationship between crystallization and polymer chain diffusion (coalescence of fibers). This includes research on the material properties of PLA polymers to tune them for FFF processing and controlling the thermal profile during printing. Srinivas et al. has already found that PLA molar mass and L-enantiomeric purity in combination with low print speeds can create stronger interfaces by allowing for polymer chain diffusion before crystallization during printing [23]. The polymer chain diffusion and crystallization processes are highly dependent on thermal conditions. Currently, the FFF printing process has a highly complex and variable thermal profile based on printing parameters and the geometry of the part. More work needs to be done to decrease the variability of the thermal profile the part is

experiencing to standardize results and give the user better information in selecting parameters for optimal properties. Current slicing software used to interface with the printer and print parts is optimized for aesthetics and time to produce a print, not consistent mechanical properties. Pursuing research in this area will hopefully result in PLA materials with stronger welds and the ability to tune processing parameters for reliable mechanical properties. Both areas are necessary to create functional PLA devices and products using FFF.

3.5 Conclusions

This study demonstrates that the print orientation and direction of fibers in respect to loading have the largest impact on mechanical properties in FFF materials due to weaknesses at the weld. Annealing is explored as a potential post-processing method to improve strength at the weld. Annealing above T_{cc} increases crystallinity, while having minimal impact on porosity. However, while crystallinity increases tensile strength in injection molded PLA, strength of FFF PLA either decreases or remains constant, suggesting that co-crystallization across the weld does not occur. AFM images support this finding showing weld interfaces between printed fibers are still visible after annealing above T_{cc}. During annealing, spherulites grow into the bulk of the fiber instead of across the weld interface. Importantly, annealing below T_{cc} shows a moderate but significant increase in tensile strength, while not impacting porosity or crystallinity. AFM images show that the as-printed interface between fibers is not fully cohesive but

annealing below T_{cc} heals the as-printed interface resulting in an increase in tensile strength. While annealing has some promise for improving strength at the weld, more research is needed on the formation of the weld and improving fiber coalescence to improve the mechanical properties of FFF PLA and decrease anisotropy between printing directions.

4. Effect of print processing and post-process annealing on PEEK mechanical properties

4.1 Introduction

Poly(aryl-ether-ketones) have seen wide interest in high performance applications across numerous industries including aerospace and biomedical applications. Of these, PEEK (poly-ether-ether-ketone) is possibly the most prevalent, due to its excellent mechanical properties and chemical inertness when fully crystallized, making it suitable for a wide range of operating conditions.[1]

There has been significant recent interest in additive manufacturing custom biomedical implants using PEEK, in particular with fused filament fabrication (FFF) and laser sintering.[2] However, recent efforts with FFF have been let down by poor weld strength between printed filaments that results in highly anisotropic behavior and poor overall part performance.[3-5] Methods to improve the adhesion between printed filaments have so far come up short, with annealing procedures and surface treatments not significantly improving the weld strength of FFF-PEEK parts.[6, 7]

Investigations on the autohesion behaviour of PEEK[8] and other semicrystalline polymers[9-11] outside of additive manufacturing methods has demonstrated that the crystallization of PEEK can inhibit the welding of PEEK surfaces above Tg, with processing parameters requiring that surface crystallization is either avoided or destroyed before strong welds can form.[12, 13] However, the mechanics of PEEK autohesion have not yet been applied in the context of FFF. Understanding the

competing kinetics of weld formation and crystallization in FFF-PEEK is made much more difficult by the complex crystallization behavior of PEEK,[14] the highly non-isothermal nature of FFF[15, 16] and the effect of flow induced crystallization on PEEK crystallization kinetics.[17-19]

This study uses a dual approach of directly imaging the PEEK microstructure at the welds between filaments with atomic force microscopy (AFM) in conjunction with characterization of the weld strength in tension and Mode III crack opening (tear testing) and bulk crystallization kinetics. These results are then compared to typical sample geometries for tensile testing (a D638 Type V dogbone and a cylinder). The combination of macroscale and nanoscale characterization methods aims to establish how the kinetics of PEEK crystallization and weld formation interact, and whether the weld strength of FFF-PEEK can be improved by carefully controlling the thermal history of the printed part.

4.2 Materials and Methods

4.2.1 Fused filament fabrication of PEEK

PEEK (Solvay, USA) cylinders, 35 mm tall and 40 mm in diameter with a single layer wall thickness were sliced using Simplify 3D (Figure 17a) and printed using Aon M2 Industrial 3D printer. PEEK filament was placed in a drying oven for at least 4 hrs at 150°C before printing to remove moisture. Cylinders were printed at multiple chamber

temperatures (Tch) to vary the bulk crystallinity of the print: 70°C, 100°C and 130°C (Figure 17b-d). All other print parameters were kept constant and are given in Table IV.

Table IV: Fixed print parameters for fused filament fabrication of PEEK cylinders and dogbones used for testing.

Sample	Parameter	Value
All samples	Nozzle Temperature	395°C
	Build Plate Temperature	180°C
	Print Speed	1500 mm/min
Large diameter cylinders	Nozzle Diameter	0.25 mm
	Layer Height	0.175 mm
Dogbones and small diameter cylinders	Nozzle Diameter	0.6 mm
	Layer Height	0.125 mm

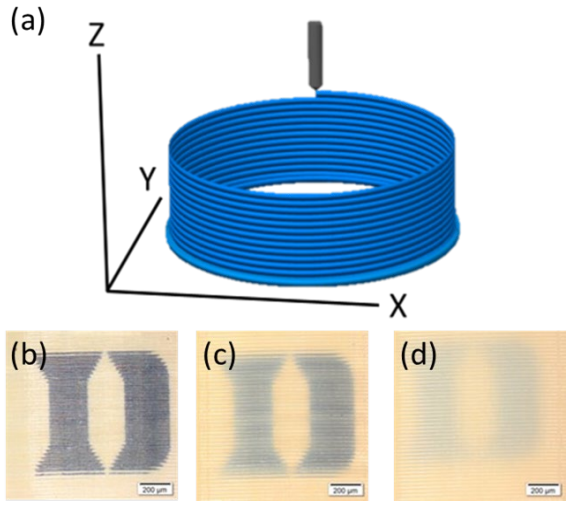

Figure 17: (a) Schematic of Simplify3D "vase mode" continuous spiral toolpath to create FFF large PEEK single-walled cylinder. Optical images displaying opacity of as-printed cylinders with (b) 70°C, (c) 100°C, and (d) 130°C build chamber temperatures. Scale bars are 200 μm.

Additional dogbone and small diameter single-walled cylinder (70 mm tall and 11.5 mm diameter) tensile geometries were printed in 70°C and 130°C build chamber temperatures with other print parameter in Table IV. The dogbone samples were D638 type V dogbones with a 3mm thickness and printed flat in the XY plane on the build plate so that printed fibers were parallel to tensile testing direction (Figure 18a-b). The single-walled VM cylinders were printed upright using a spiralized "vase-mode" toolpath so that printed fibers were perpendicular to tensile testing direction (Figure 18c-d). For tensile testing, the ends of the open cylinder were reinforced with an epoxy (SigWong, China) tab to create a solid grip section. A silicone mold (Diamond Driven Liquid Silicone Compound) with the desired epoxy tab dimensions was created. The silicone mold was filled with epoxy resin, VM cylinders were placed upright in the mold

and the mold was placed in an oven at 60°C for 3 hours to cure the epoxy. A hole was drilled in the cured epoxy to allow air to escape and the procedure was then repeated on the other side to create epoxy tabs on both sides of the sample.

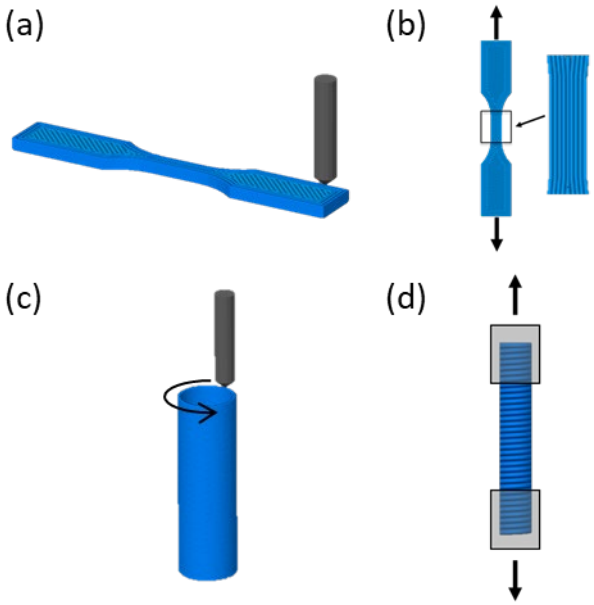

Figure 18: Printing orientation and testing schematic for D638 Type V dogbones in flat print orientation (a) that are tensile tested with printed fibers parallel to direction of loading (b), hollow cylinder that is printed in "vase mode" (VM) (c) with reinforced epoxy ends for tensile testing with printed fibers perpendicular to direction of loading (d)

4.2 Differential scanning calorimetry

The crystallinity of the filament, as printed, and annealed was determined using DSC (TA Discovery 2500). Unless otherwise specified, approximately 10 mg was cut from the thin walled cylinder samples and heated at 10°C/min in a nitrogen environment. The percent crystallinity was determined from the first pass ΔH_m divided

by the theoretical ΔH_m of 130 J/g for 100% crystalline PEEK[42]. Calibration was performed with an Indium standard.

4.3 Tear testing

Tear testing of the weld strength in the cylindrical sample was conducted following the protocol outlined in Seppala *et. al.*[43]. Samples were cut from the printed cylinder to be 5 mm wide and 60 mm long with the fiber direction aligned with the long axis of the sample (Figure 19a). A precrack was initiated along a weld in the center of the sample using a sharp razor.

Tear testing was conducted using an RSA G2 DMA (TA Instruments, USA). Samples were pulled at a constant rate of 50mm/min to induce Mode III crack growth along the weld (Figure 19b) until the weld had completely torn. The tearing was calculated according to

$$T = \frac{2F}{w} \qquad \text{Eq. 1}$$

Where F, is the average force during stable tearing and w is the width of the weld. Like Seppala *et. al.*, we calculate the nominal tearing energy using the overall wall thickness, w_0 and the true tearing energy using the actual weld thickness, w_t which is measured 10 locations using optical images of the cylinder wall cross-section. The measured thicknesses of the walls and welds for each of the chamber temperatures are given in Table IVTable V. For the remainder of the study, the quoted tearing energy values are the true values, allowing comparison to film samples.

Table V. Average dimensions of the fiber width and weld length in the as-printed samples at three chamber temperatures. Error values reflects the standard distribution across a sample of 10 welds.

Process Temperature (°C)	Wall Thickness, w_0 (μm)	Weld Thickness, w_t (μm)	w_t/w_0
T_c = 70	356 ± 17	263 ± 13	0.74 ± 0.05
T_c = 100	355 ± 11	277 ± 5	0.78 ± 0.03
T_c = 130	338 ± 9	258 ± 8	0.76 ± 0.03
T_A = 148	370 ± 9	268 ± 7	0.72 ± 0.03
T_A = 180	352 ± 13	267 ± 8	0.76 ± 0.04
T_A = 148 and 180	371 ± 12	275 ± 10	0.74 ± 0.03

4.4 Tensile Testing

The tensile strength of the printed large diameter (40 mm) cylinders was determined through monotonic tensile testing (Test Resources 830EL63) of strip samples cut out of the cylinders. A razor blade cut perpendicular to the weld was used to create the strip subsections (Figure 19a). The strips were 10 mm wide and between 10-35 mm long (total height of cylinder), depending on if cracks formed along the welds during cutting. The part of the sample placed in the tensile grips was reinforced with epoxy (J-B

Weld) (Figure 19c). Small diameter (11.5 mm) cylinders were tested as printed with epoxy reinforced grip section ends. Printed tensile dogbones were tested as printed without further modification.

All tensile samples were tested at a displacement rate of 1 mm/min until failure. Failure is defined as the fracture of the printed welds in the sample resulting in a decrease in stress. The cross-section dimensions of samples were measured with calipers before testing. Strain was measured by marking tracking points on the sample before testing and using a video extensometer system. Strain for the small diameter VM cylinders was calculated based on the distance between the epoxy reinforced sections and displacement of the crosshead.

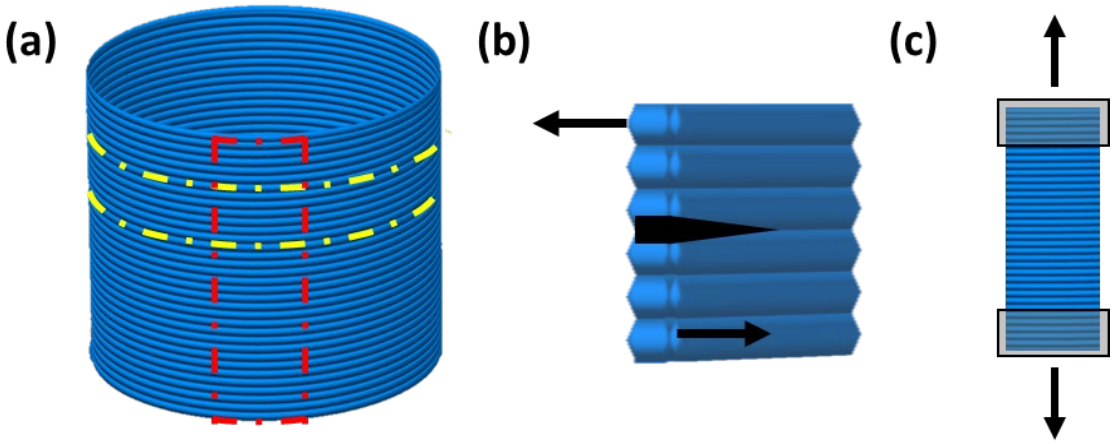

Figure 19: (a) Schematic of sample cuts for tear testing (yellow) along the weld lines and tensile testing (red) perpendicular to the weld. (b) Tear testing setup with a pre-crack along a weld line and the two free ends pulled apart to drive Mode III crack propagation. (c) Tensile testing setup with grayed regions representing the epoxy reinforced grip section.

4.5 Atomic force microscopy (AFM)

Atomic force microscopy (AFM) scans were collected across the weld region between fibers of select samples to observe polymer structure and crystallinity at the interface between fibers. To prepare samples for AFM, sections were cut from the printed cylindrical samples using a diamond saw, and then a surface for AFM analysis that included the weld interfaces (Figure 19b) between three fibers was wet-sectioned at room temperature with a UC7 Ultramicrotome (Leica, Germany) to produce a smooth surface, with an R_a = 0.56 nm as measured by AFM in the amorphous regions of the samples. The cutting direction during sectioning was perpendicular to the weld interface to preserve the weld structure.

AFM images were acquired in tapping mode using a Cypher ES (Asylum Research, USA) atomic force microscope (AFM) across the weld region of select samples, Figure 19b, to observe the change in morphology of crystalline domains, if any, at the weld interface. Measurements were acquired at room temperature with a silicon cantilever (AC240, Olympus) that has a nominal tip radius of 7 nm that was driven on resonance using BlueDrive(TM). The measurement parameters used are provided in the caption of the relevant data set.

4.3 Results and Discussion

The following results first examine the bulk crystallinity and mechanical strength of the large diameter cylinders as printed welds at three different chamber temperatures in tension and Mode III crack opening conditions. AFM imaging of the distribution of crystallinity in the sectioned fibers is then conducted to understand the significant decrease in weld strength with increasing chamber temperature. Annealing procedures are developed to improve the strength of the PEEK welds post-print. Finally, bulk crystallinity and mechanical strength measurements are repeated in two additional sample geometries.

4.3.1 Influence of chamber temperature on crystallinity and weld strength

The large diameter cylinders printed at the three chamber temperatures were first analyzed in DSC to establish the bulk crystallinity of the as-printed samples. Examples of the heat flow traces acquired on heating are provided in Figure 20. A clear transition in cold crystallization behavior can be observed above the Tg of the as-printed PEEK with increasing chamber temperature. The cold crystallization enthalpy peak is strongest for the samples printed at Tch = 70°C, still present for the samples printed at Tch = 100°C, and no cold crystallization is observed for the Tch = 130°C samples.

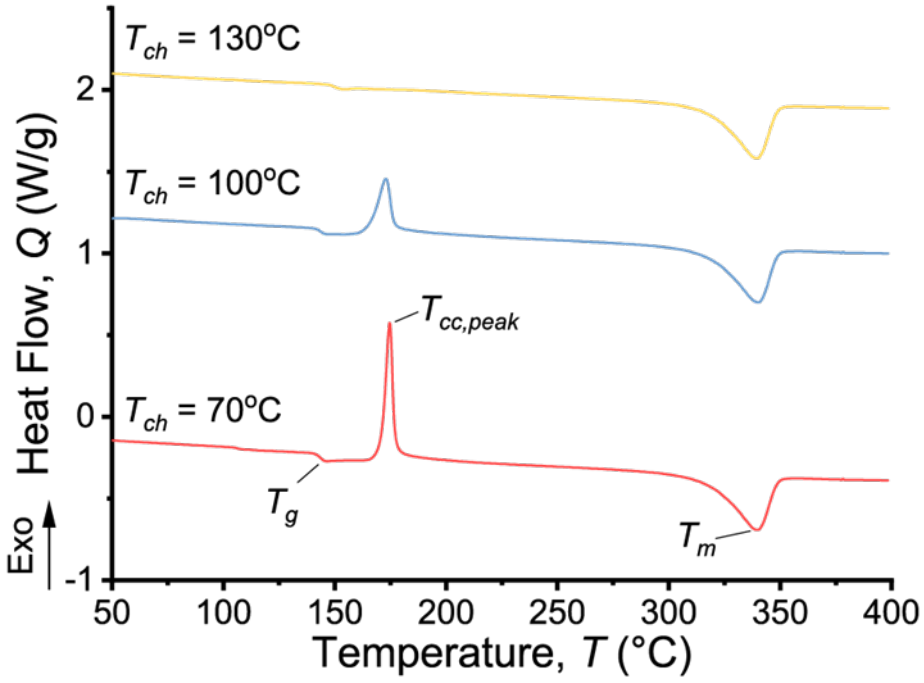

Figure 20: Example DSC traces of FFF-PEEK printed at three chamber temperatures.

Measurement of the enthalpy of cold crystallization and the melt enthalpy allows for a calculation of the as-printed crystalline fraction (Table VI). Calculation of the as-printed sample crystallinity shows very little crystallinity for the samples printed at 70°C and 100°C whereas the samples printed at 130°C has completely crystallized. The increase in crystalline fraction for the T_{ch} = 130°C is accompanied by an increase in the measured T_g of the sample. These results are consistent fundamental understanding that shock cooling of a polymer sample does not allow for crystallization and leads to cold crystallization as the sample is heated past T_g in a DSC run. Thus in these data, the lower chamber temperatures allowed limited crystallization during printing, while the highest

chamber temperature was close enough to T_g to allow full crystallization to occur in the as-printed sample.

Table VI: DSC characterization of the as-printed crystallinity for each of the three build chamber temperatures tested. Error represents one standard deviation. 3 samples were tested for each chamber temperature.

Build Chamber Temp (°C)	Glass Transition Temperature, T_g (°C)	Cold crystallization onset temperature, $T_{cc,onset}$ (°C)	Cold crystallization peak temperature, $T_{cc,peak}$ (°C)	Melt Temperature, T_m (°C)	Enthalpy, ΔH (J/g)	As-printed crystalline fraction (%)
70	143.2 ± 0.1	171.0 ± 0.2	174.7 ± 0.1	339.6	10.3 ± 2.02	8 ± 2
100	143.0 ± 0.3	165.6 ± 0.3	172.8 ± 0.04	339.7	10.1 ± 3.29	8 ± 3
130	149.2 ± 0.3	-	-	339.5	42.3 ± 0.42	32 ± 2

To compare the strength of the crystalline and amorphous welds, Mode III crack opening and tensile experiments are performed on the PEEK samples for each of the three chamber temperatures tested: 70°C, 100°C and 130°C. Examples of the tearing curves and tensile stress-strain curves acquired for each chamber temperature is provided in Figure 21(a) and (b) respectively. Stable tearing can be observed on the welds printed with the 70°C chamber temperature at a steady-state force of approximately 4 N required to maintain crack growth. For the samples printed at the higher temperatures, crack growth was unstable, with stick-slip tearing indicating brittle fracture along the weld. Isolated periods of stable crack growth can be observed in the 100°C force-displacement curves, and generally require high forces to initiate unstable crack growth. The resulting nominal tearing strength calculated from averaging the

force over the draw distance shows a dramatic decrease in weld strength as the chamber temperature is increased. The tensile stress-strain curves show that samples printed at Tc = 70 °C are strongest while samples printed at Tc = 130 °C particularly weak in tension. Quantifying the elastic modulus and ductility of the samples in tension is complicated by the non-ideal sample geometry and the apparent interfaces of the printed layers on the measurement of strain with the video extensometer used in this study. The decrease in weld tearing strength with chamber temperature is correlated to the change in ultimate tensile strength (Figure 21c), suggesting that for the tested sample geometry, the strength of the weld (as measured by trouser tear experiments) controls the overall strength of the sample in tension. It should be noted while the trouser tear test randomly samples welds to be tested for tearing strength measurements of UTS in tension applies a load across multiple welds, the weakest of which will define the UTS. The disconnect between expectations from bulk PEEK mechanical properties and the performance of FFF-PEEK with increasing chamber temperature and crystallinity suggests the processing is responsible for the poor mechanical properties. The connection between weld strength and UTS indicates that local changes at the weld between the printed fibers during processing may be primarily responsible for the poor mechanical properties observed in the highly crystalline samples. To examine whether the mechanism causing poor mechanical strength can be identified, AFM is used to directly examine local weld structure.

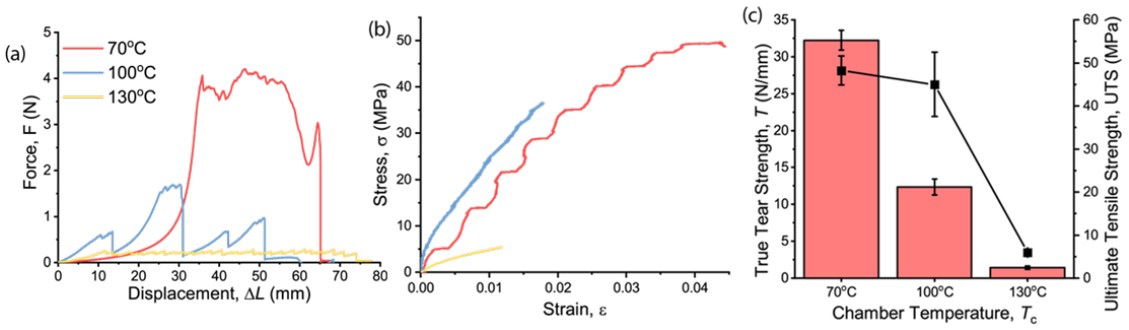

Figure 21: Tear and tensile strength of large diameter welds including (a) Representative plots of force as a function of grip displacement for Mode III tear testing of welds in FFF-PEEK. Each curve demonstrates typical behavior for samples printed at each of the three chamber temperatures. (b) Stress-strain curves of samples tested in tension for each of the three chamber temperatures. The oscillatory behavior observed for T_c = 70 °C is the result of the printed layers interfering with the video extensometer measurement of strain. (c) True tearing strength and UTS for each of the three chamber temperatures tested. Error bars represent one standard deviation. For tearing energy measurements, at least 5 samples were tested for each T_c. For UTS measurements, 3 samples were tested for T_c = 70 and 100 °C whereas 2 samples were tested for T_c = 130° C due to the fragility of the samples printed at T_c = 130° C.

4.3.2 AFM of PEEK weld crystalline microstructure

To understand local changes in the weld, the first step was to directly image the distribution of crystallinity across a fiber to determine the distribution of spherulites by using AFM to map the locations of the spherulites and directly the weld directly at the nanoscale to see the extent of weld formation, if any. A model sample printed under conditions to promote moderate crystallinity was sectioned and imaged first with optical microscopy under DIC (differential interference contrast) as shown in Figure 22a to obtain a high-level map of crystallinity followed by targeted AFM for higher resolution and surface detail (Figure 22b-c) across regions of interest.

The optical image under DIC contrast conditions indicates an irregular distribution of crystallinity throughout the printed specimen (Figure 22a). Here the crystalline domains manifest themselves in the height data channel due to the rough local surface topology compared to the relatively featureless amorphous regions of the polymer. It is expected that during sectioning that the crystalline domains fracture along preferential planes depending on the orientation of the crystallite relative to the cutting direction. As such the individual lamellae are exposed with surface normal that are not necessarily coincident with the surface normal of the cutting plane. In comparison the amorphous regions have no preferential fracture direction and appear relatively smooth. The horizonal streaks that can be observed are due to cutting marks from the ultramicrotomy. Porosity can also be observed as bright features at the weld lines between filaments.

AFM imaging across the filament, Figure 22b, shows that a higher density of crystalline domains can be observed in the center of the filament with the density of spherulites gradually decreasing radially until there is minimal crystallinity in the fiber bulk with approximately 15 μm of the weld lines. However, significant crystallinity can be observed along both weld lines. Additional imaging of one of the weld lines (Figure 22c) confirms that the weld line is almost entirely crystalline. The gradual decrease in crystallinity from the fiber center outwards can be explained through an increase in the local cooling rate reducing the time for crystal growth before the filament decreases

below Tg and molecular motion is ceased[44]. However, the highly crystalline weld line suggests that the nucleation and growth of crystallites at the interface is occurring much faster than crystallization in the bulk of the neighboring fibers.

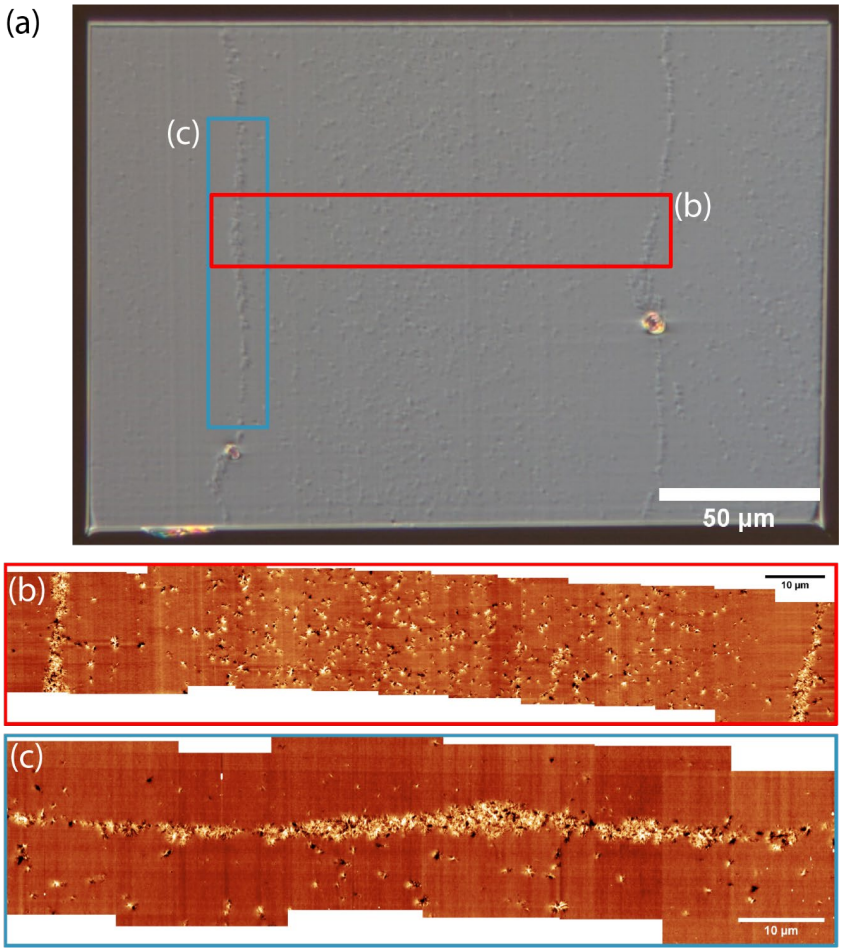

Figure 22: Images of weld interface including (a) DIC optical image of ultra-microtomed surface for a single printed filament and its welds with neighboring fibers. The area imaged with AFM are indicted by the colored rectangles. Texture in the image is the result of exposed spherulites. (b) Stitched AFM height images across the central filament from one weld interface to the other within the region indicated by the red rectangle in (a). (c) Stitched AFM height images of the weld interface within the blue rectangle indicated in (a). The measurement parameters are $A_{0,3}$ = 3.2 nm, A_3 = 2.1 nm, $f_{0,3}$ = 1221.7 kHz, Q_3 = 584.99

Further investigation on another sample printed with both amorphous and highly crystalline regions indicates that the weld interface is consistently more crystalline than the fiber bulk. A bright field optical image of the ultra-microtomed surface in Figure 23a shows a significant variation in crystallinity at the macroscopic scale along the z-axis as a result of the variation in the temperature of the hot end and proximity to the heated build plate. To interpret Figure 23a, note that the predominantly amorphous regions of the part are transparent and therefore dark in the optical image, while the spherulites scatter the incident light, making crystalline regions opaque.

Thus the optical image in Figure 23a illustrates a transition across the printed part such that the base of the sample near the heated plate is predominantly crystalline while regions further removed transition to being predominantly amorphous. The change in degree of crystallinity is expected to be related to the local thermal history, with layer-by-layer variation of crystallinity likely due to changes in the temperature of the nozzle. From this cross-section, locations that are representative of each of the amorphous, partially crystalline, and crystalline regions are identified and marked with (b), (c) and (d) in Figure 23a.

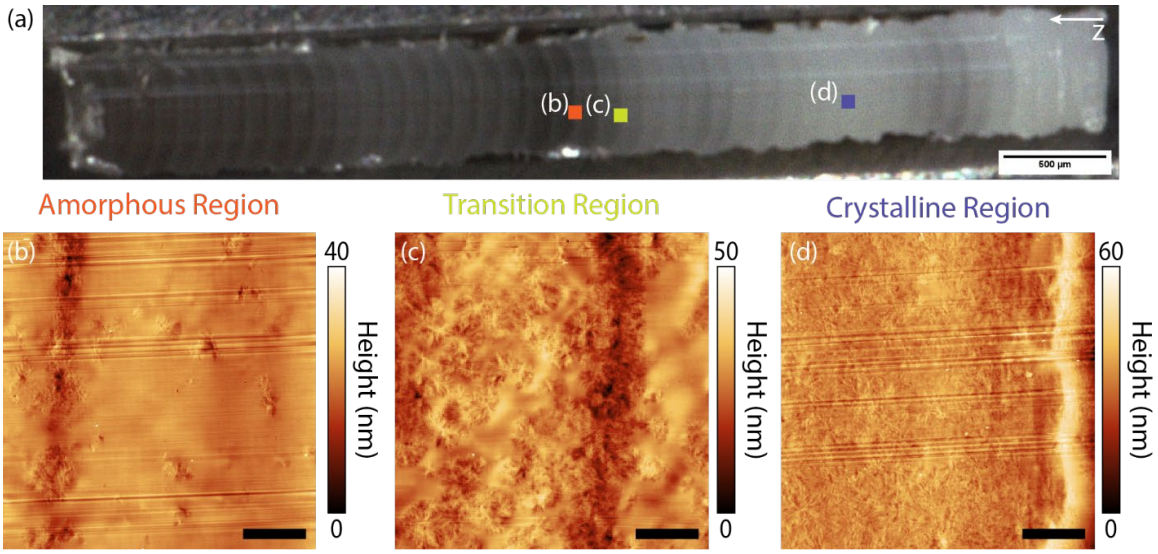

Figure 23: AFM images of crystallinity transition regions including (a) Large scale optical image of the microtomed cross-section of the FFF printed sample. The printing direction from the build plate is indicated with the arrow labelled z. White, opaque regions indicate highly crystalline regions. Dark transparent regions indicate amorphous regions. The areas targeted for AFM imaging are indicated with colored squares. (b) Weld interface in the amorphous region of the sectioned surface. Isolated spherulites are observed in the bulk of the filament with moderate interface crystallinity. (c) Weld interface in a transition region with moderate crystallinity. Higher spherulite density in the bulk is observed compared to the amorphous region, with a fully crystalline interface (d) Weld interface in a highly crystalline region of the sectioned surface. Any crystallinity at the weld is nearly indistinguishable from the bulk crystallinity. Black scale bar in (b-d) indicates 4 µm. Black arrows in (b-d) indicate the location of the weld line between printed layers. The typical AFM measurement parameters are $A_{0,1}$ = 56.1 nm, A_3 = 37.0 nm, $f_{0,3}$ = 62.205 kHz, Q_3 = 170.44

AFM height images on each of the regions indicated in Figure 23a are collected and given in Figure 23b-d, where each region contains a weld. The weld interface in Figure 23b within the amorphous region shows sparse spherulites in the bulk of the filament. At the interface, a higher spherulite fraction can be observed. Near an interface in the transition region the density and size of the spherulites increase (Figure 23c), with an associated increase in the crystalline fraction at the weld line. In comparison to the

amorphous region, the spherulites are more spherical and symmetric suggesting longer growth times. In the highly crystalline region, the weld interface is indistinguishable from the bulk crystallinity which has a dense interconnected number of spherulites (Figure 23d).

That the interface is always more crystalline than the bulk suggests that the nucleation and growth of crystallites at the interface occurs more quickly and/or for longer times than the nearby bulk material. Three possible explanations are: 1) free surface mediated crystallinity in which the added mobility of polymer chains at the free surface allows for premature and rapid crystallization compared to the polymer bulk,[45], [46] 2) different thermal gradients at the surface layer as result of radiant heat transfer from the printer nozzle, or 3) heterogenous crystal growth at the weld interface due to trapped impurities or surface defects.

Figure 21 shows that the weld strength decreases with increasing chamber temperature, suggesting that at higher chamber temperatures the PEEK crystallizes more rapidly than welds between printed fibers can effectively form. As the chamber is reduced in temperature, the cooling rate of the PEEK is increased such that the printed filament spends less time in the temperature range (approx. 180-240°C) for fast PEEK cold crystallization where the crystallization half time, $\tau 1/2$ can be less than a second.[47], [48]

4.3.3 Annealing of PEEK

The strong weld strength that results from printing with T_{ch} = 70 °C presents an opportunity to produce strong, fully crystallized additively manufactured PEEK components by using a post-print anneal to cold crystallize the printed parts and induce co-crystallization across the weld. While the amorphous FFF-PEEK demonstrates good mechanical properties, the full mechanical strength and chemical inertness of bulk PEEK is realized when the polymer is fully crystallized.[2], [49], [50] As such, it would be beneficial to examine whether a printing and post-processing procedure that allows crystalline FFF-PEEK to realize its full potential is possible and obtain properties comparable to bulk crystalline PEEK is possible. The major barrier to strong, crystalline, FFF-PEEK parts, as laid out in Sections 4.3.1 and 4.3.2 is the premature crystallization causing a barrier to weld formation during printing, preventing effective chain entanglement[14], [18] and co-crystallization[51] across the welds between fibers.

The best possible environment for co-crystallization requires that the polymer chains near the weld are returned to equilibrium conformations and allowed to entangle during annealing before crystallization occurs. Therefore, a two-step annealing process will also be investigated, where a low temperature annealing step above Tg, but below Tcc is first used to encourage chain diffusion and weld healing, followed by a high temperature annealing step above Tcc to induce cold crystallization. It is clear from Figure 20 that the low temperature annealing step must occupy a very small range

between the Tg and Tcc of the printed PEEK. Exploratory annealing at a range of temperatures in the DSC (Figure 24a) over 12 hrs demonstrates the thermally activated nature of cold crystallization, with crystallization observed above 150°C (Figure 24b), but no significant change below 148°C. Therefore, an annealing temperature to relax the weld structure but prevent crystallization should be below 150°C, but above the as-printed Tg of 143 °C so that the chains have at least some mobility. After the annealing step below 150°C is conducted to promote weld formation, an additional crystallization step above 150 °C will be used to fully crystallize FFF-PEEK samples printed with Tch = 70 °C. For the following two-step annealing studies an initial annealing temperature of 148 °C is maintained for 6 hours for weld formation, followed by an anneal 180 °C for another 6 hrs to promote cold crystallization. In addition, other samples are annealed at either 148 °C or 180 °C for 12 hours for comparison to the two-step annealing procedure. The weld and tensile strength of the annealed samples is then compared to the as-printed samples.

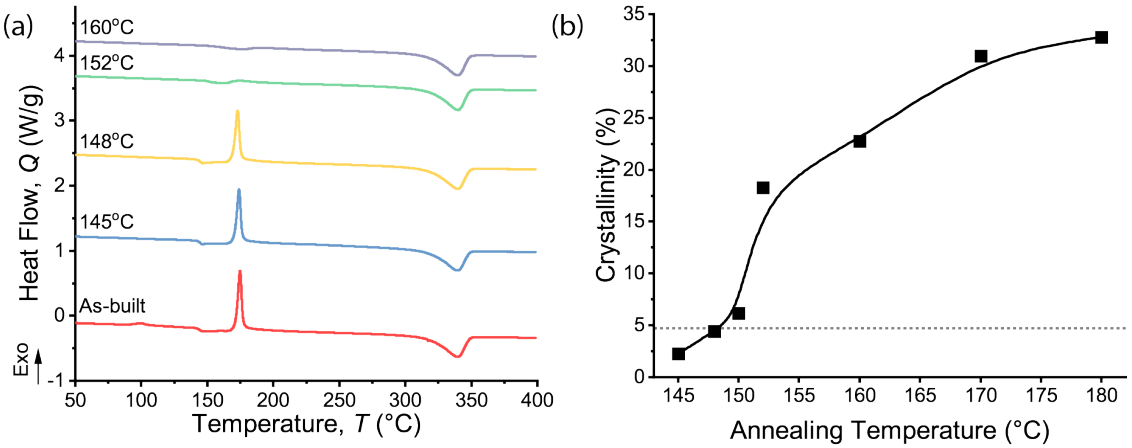

Figure 24: (a) DSC traces of PEEK samples printed with Tc = 70°C upon heating at 10°Cmin-1 after annealing at the indicated temperatures for 12 hrs. (b) Resulting crystalline percentage as a result of annealing after 12 hrs annealing at an annealing temperature TA. The dotted gray line indicates the measured crystallinity of the bulk polymer after printing at Tc = 70°C. The black line is a guide to the eye.

The tensile and tearing strength of the single-step and two-step annealed FFF-PEEK samples is provided in along with the as-printed samples at each of the three chamber temperatures.

The two-step annealed, crystalline PEEK demonstrates a significant 6-8× improvement in tensile strength over the comparably crystalline samples printed at Tch = 130°C (Figure 25a). The two-step annealed PEEK also shows slightly improved mechanical properties than the fully crystalline PEEK one-step annealed at 180 °C. The measured UTS of 49 MPa for the two-step annealed, crystalline sample remains much lower than the expected UTS of 95 MPa for bulk Ketaspire™ PEEK, which is likely due to the notch sensitivity of PEEK[52]. However, the dramatic increase in strength compared to the as-printed PEEK with Tch = 130 °C highlights the ability of two-step

annealing to dramatically improve the strength of crystalline PEEK compared to PEEK that is allowed to crystallize during printing. Further optimization of printing and two-step annealing parameters should further improve the strength of crystalline FFF-PEEK. The major increase in strength demonstrated here with two-step annealing should greatly assist the application of fully crystalline FFF-PEEK in functional, load-bearing devices. Further the identification of a very small 'goldilocks' zone between Tg and ~150 °C that enables relaxation without crystallization in PEEK may explain why previous annealing studies have had limited success with improving the strength of PEEK through annealing[26], [51]. The ultimate goal with two-step annealing will be to achieve fully crystalline FFF-PEEK that can match bulk PEEK strength, but would likely require modification of the part geometry to minimize porosity and avoid the notch sensitivity of crystalline PEEK.

Comparing the tear strength of the samples printed with Tch = 70°C to annealed samples shows a decrease in tear strength with annealing (Figure 25b). The sample annealed at 148°C for 12 hrs also shows an accompanying decrease in measured crystallinity, suggesting that the annealing has allowed for relaxation of non-equilibrium conformations of the sample printed at Tch = 70°C. Meanwhile the sample printed with Tch = 100°C has an apparently similar crystallinity to the sample printed at Tch = 70°C, but exhibits dramatically worse tearing strength. If relaxation of non-equilibrium conformations formed during printing with Tch = 70 °C contributes to the measured

enthalpy during heating above Tg, relaxation of the non-equilibrium conformations could be convoluted into the quantification of crystalline fraction in the sample printed at Tch = 70°C. and explain the discrepancy in mechanical performance compared toMeanwhile the sample printed at Tch = 100°C, despite a similar apparent crystalline fraction, to the sample printed with Tch = 70 °C is much weaker as crystallization that occurs at the slightly higher chamber temperature limits weld strength.

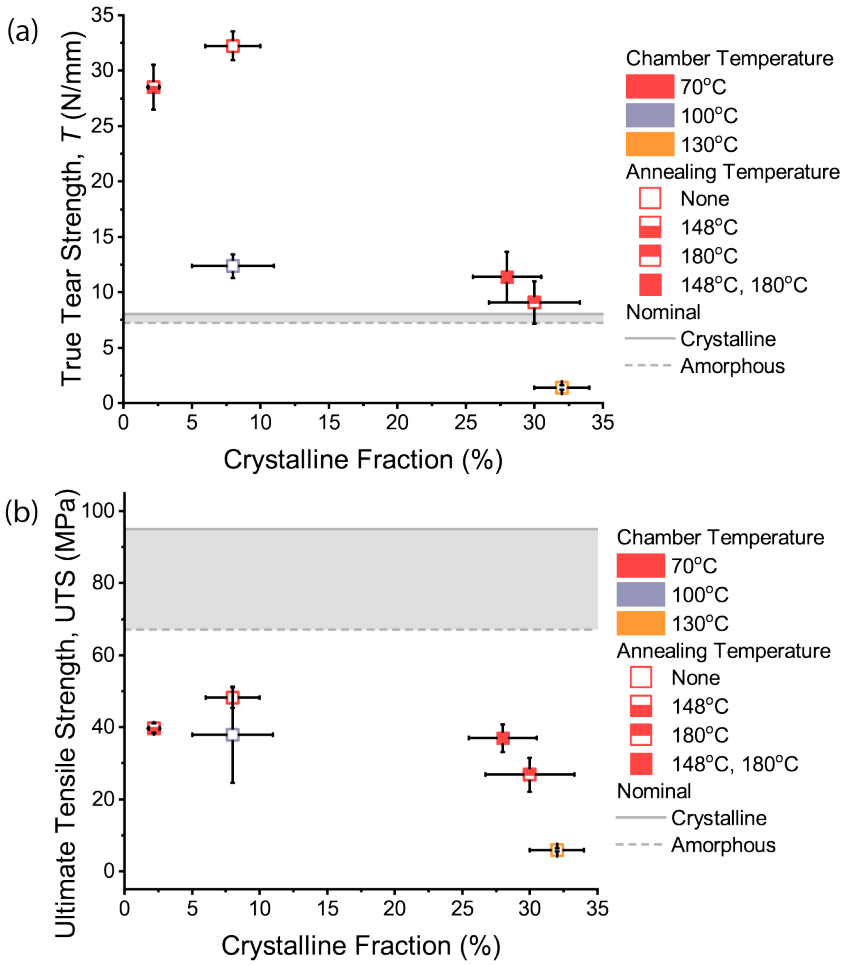

Figure 25: Comparison of (a) ultimate tensile strength and (b) weld tearing strength as a function of bulk crystallinity as measured by DSC. All annealing is conducted for a total of 12 hrs and all annealed samples are printed with Tch = 70 °C. Annealing procedures that use multiple temperatures anneal first at 148°C followed by 180°C. The nominal tensile strength for amorphous and crystalline PEEK is estimated from Chivers et. al.[49] **and the data sheet for Ketaspire PEEK™ (Solvay, USA) respectively. The nominal tearing energy for amorphous and crystalline PEEK is measured from the tearing energy of 30µm thick, amorphous, PEEK (Ketaspire™, Solvay, USA) films before and after cold crystallizing at 180°C for 12 hrs. At least 5 samples are tested for the tearing energy data and the error bars represent that standard deviation.**

4.3.4 Crystallinity and tensile strength of bulk PEEK samples

While the large cylinders were good samples for investigating the crystalline structure and tear strength of individual welds, the tensile samples were not ideal due to the mechanical deformation caused by cutting samples out with a razor blade and the curved nature of the samples. To produce data that could be better compared to traditional tensile data, samples were printed with ASTM D638 Type V dogbone dimensions. VM cylinders are less traditional but more "printer-friendly" structures for creating samples with fibers oriented perpendicular to loading direction. They were printed in a minimum build chamber temperature of 70°C and maximum build chamber temperature of 130°C. However, the samples printed in T_{Ch} = 70°C did result in low crystallinity. Unlike the large diameter cylinders, all dogbone and VM cylinder samples had crystalline fractions > 30%, even at T_{ch} = 70°C, Table VII

Table VII: Tensile strength for PEEK from dogbone and small diameter VM cylinder geometries with DSC crystallinity of samples

Sample geometry	Chamber temperature (°C)	Average UTS ± StDev (MPa)	Failure strain ± StDev (mm/mm)	Crystallinity ± StDev (%)
Dogbone	70	76.1 ± 1.4	0.04 ± 0.01	32 ± 0.1
n = 3	130	74.5 ± 12	0.03 ± 0.01	31 ± 0.6
VM cylinder	70	48.4 ± 6.7	0.04 ± 0.01	31.3 ± 0.8
n = 6	130	64.8 ± 12	0.06 ± 0.04	30.6 ± 0.5

While the crystallinity was consistent, the tensile behavior of the samples was dependent on sample geometry and build chamber temperature. Dogbones printed in

both chamber temperatures had similar UTS of 76.1 MPa (70°C) and 74.5 MPa (130°C), Figure 26a. The PEEK VM cylinder had significantly lower UTS of 48.4 MPa in a 70°C build chamber temperature compared to 64.8 MPa in a 130°C build chamber temperature, Figure 26b. Overall, the dogbone geometry with fibers oriented parallel to the testing direction had higher UTS than the VM cylinder (fibers perpendicular to testing direction). There was not a significant difference in the failure strain in different build chamber temperatures for each of the PEEK sample geometries.

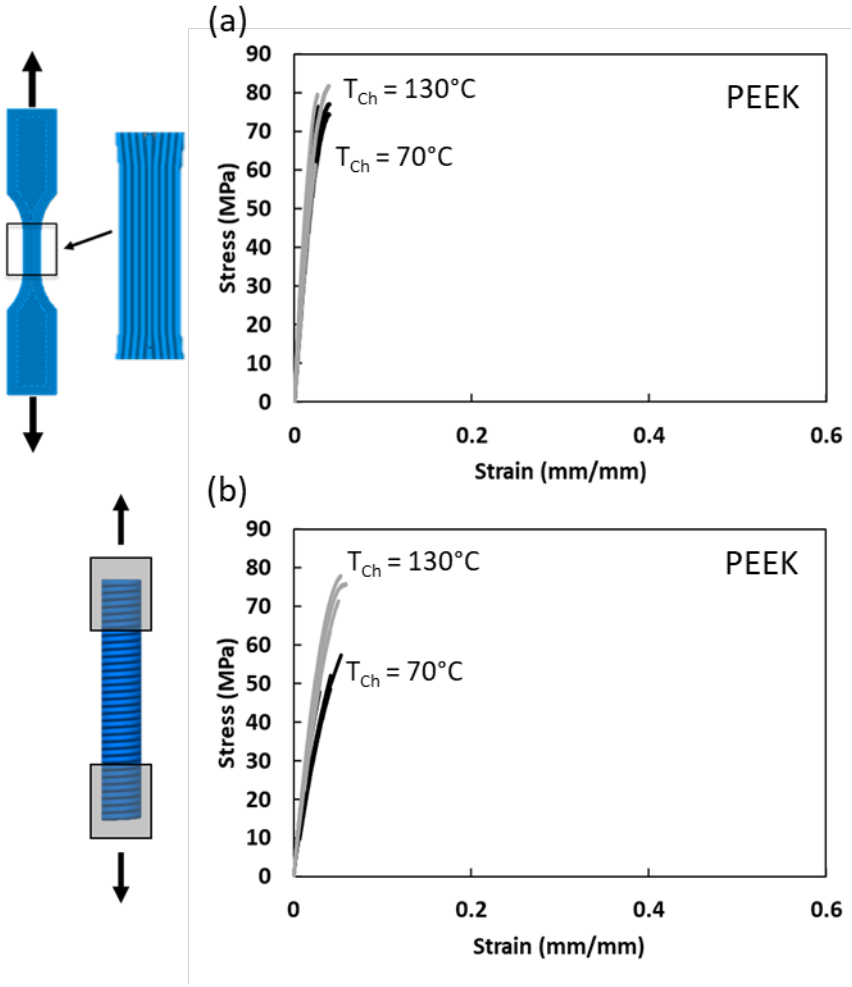

Figure 26: Tensile stress-strain curves for dogbones (a) and large diameter VM cylinders (b) printed in a 70C chamber temperature (black) and 130C chamber temperature (gray)

While the build chamber temperature for these samples was the same as the large diameter cylinders, changes in other parameters including the nozzle diameter and toolpath created a different thermal history, as reflected by the differences in crystallinity. Additionally, the higher build chamber temperature resulted in higher UTS for the VM cylinder samples, opposite of the large diameter cylinder tear and tensile

results. These samples had a larger thermal mass due to the increased nozzle size and they were likely exposed to higher temperatures for longer as the smaller diameter subjecting the previously printed layer to residual heat from the hotend while the next layer was printed. This would cause the printed layer to remain at a temperature closer to the melt temperature as the next layer is deposited and slow crystallization in the printed fiber as crystallization half time increases as the temperature approaches the melt[48], [53]. Further investigation is needed to understand the relationship between crystallization and polymer chain diffusion from the glass transition temperature to the melt temperature and a printer with the ability to hold the chamber/printed material at a higher ambient temperature is required. One potential challenge of printing PEEK at higher temperatures closer to melt is the increased flow that could negatively impact the ability to print consistent and accurate part dimensions.

4.4 Conclusions

PEEK has long been an attractive material for the additive manufacturing of medical implants due to its exceptional mechanical properties and chemical inertness. However, PEEK components manufactured via fused filament fabrication have suffered from poor mechanical properties and anisotropy due to poor weld strength. Tearing energy measurements of FFF-PEEK samples printed at different chamber temperatures indicate that increased crystallinity in the printed PEEK decreases weld strength, contrary to expectations from bulk mechanical property behavior.

From AFM imaging of the weld zone in FFF-PEEK, we hypothesize that the crystallinity at the interface is the result of surface induced crystallization that prevents strong weld formation between FFF-PEEK filaments. One possible mechanism for the high surface is crystallinity is free surface effects. At the free surface, higher polymer mobility is observed, resulting in a reduction of local Tg and Tcc and an increase in the crystallization kinetics. During deposition of the PEEK filaments, free-surface mediated crystallization allows rapid formation of PEEK crystallites in the surface layer of the deposited filament faster than what is expected from bulk measurements of crystallization from DSC. As a result, the free surface of the deposited filament crystallizes before the next layer can be deposited. The crystallized surface layer of polymer forms a hard, immobile 'skin' that prevents weld formation between the printed layers. Therefore, the reduction of fracture toughness with increased crystallinity is expected. To address the surface crystallization the print geometry and chamber temperature is adjusted such that amorphous PEEK parts are printed. Two-step annealing, where the printed part is first annealed above Tg, but below the Tcc allows for relaxation of non-equilibrium conformations and weld healing without crystallization followed by a second annealing step above Tcc to induce cold crystallization, yields fully crystalline FFF-PEEK parts with 6-8× stronger welds than what is achieved with standard printing methods. Further investigation is required to determine appropriate annealing times for weld healing from the polymer rheology and

diffusion kinetics between Tg and Tcc. Additionally, the results in the bulk tensile samples, and improvement of UTS with the high build chamber temperature VM cylinder, warrant further investigation into slowing crystallization and improving polymer chain diffusion across the weld by raising the temperature of printed material closer to the melt either through a printer with a higher build chamber temperature (global temperature control) or through local temperature control at the hotend.

5. Effect of print processing and post-process annealing on PPSU and PEKK mechanical properties

5.1 Introduction

Numerous high-performance thermoplastics are used in medical devices. The ease of processing and high mechanical properties combined with light weight make them useful in many applications from components of pace-makers to spinal cage devices for spinal fusions along with many support devices such as bone fixture screws and plates. Many of these devices have success due to mechanical properties that are more compatible with biological properties and a low density/radiolucency that allows for better imaging compared to metallic devices. Some of these devices would benefit from more complex and difficult to manufacture features including porosity for osseointegration and/or patient specific devices that are custom for each patient case. Currently, porosity is achieved through surface modification but it does not pervade the entire device[54]. While some patient specific devices are already created with traditional manufacturing methods, 3D printing could make these devices more accessible through reduction of time and cost to manufacture[55].

For thermoplastics, there are two main 3D printing methods, powder bed fusion (PBF) and fused filament fabrication (FFF, also known as material extrusion)[7]. A couple challenges with PBF are the expense of machine and the potential waste from unsintered powder in the bed that cannot be reused. There is ongoing research relating to reuse of the unsintered powder but current research in polyamides shows changes in

the powder and a decrease in properties when using recycled powder[10]. In general, FFF is a cheaper and more common method and the one explored in this study. One particular challenge of FFF is the creation of weak interfaces between printed layers, a key component of the overall part performance. Due to the multitude of process parameter selections and the ease of printing typical tensile dogbones flat on the build plate, many studies report properties of printed fibers oriented in the direction of loading instead of exposing this weakness by testing samples with fibers oriented perpendicular to loading direction.

Polyetheretherketone (PEEK) is currently the most investigated high strength polymer in 3D printing literature with many medical device applications[3], [7]. Polyetherketoneketone (PEKK) and Polyphenylsulfone (PPSU) are two additional high-strength polymers with use in medical devices with the potential for 3D printing [7], [56], [57]. Current PEKK studies evaluate the rheological properties for extrusion based 3D printing but no data on mechanical properties of FFF PEKK [58] while there are no studies evaluating PPSU. While PEEK is the most investigated, its fast crystallization rate can pose challenges for weld formation during 3D printing [44], [51], [53], resulting in mechanical properties inferior to injection molding [12], [26], [59], [60]. In contrast, while PEKK is in the same polyaryletherketone family at PEEK, it has a lower crystallization rate [48] and PPSU is an amorphous polymer.

While it is possible to 3D print these materials, there are limited FDA regulated 3d printed high performance thermoplastic devices, only 2% of 510k cleared 3D printed, porous devices were extrusion based in 2016 and the majority of polymeric devices were created from thermosets instead of thermoplastics [61]. Further investigation is needed to overcome the mechanical property challenges of 3D printing high performance thermoplastics.

Based on current literature, it is clear that FFF print processing results in material properties differ from properties of conventionally manufactured materials. This study compares properties of alternative high-performance thermoplastics for medical devices (PEKK and PPSU) in tension and compares them to PEEK properties from the previous chapter. A key contribution of this study is a method for creating a simple single-walled sample geometry for comparing tensile properties with printed fiber oriented perpendicular to testing direction. Based on initial mechanical property results, PEKK properties are further explored by annealing as-printed samples and in tensile fatigue.

5.2 Materials and Methods

5.2.1 Print processing of samples

Dogbone and single-walled "vase mode" cylinder (VM cylinder) solid tensile samples of PEEK (Solvay, USA), PEKK-C 70/30 copolymer (3DXtech, USA), and PPSU (Solvay, USA) were printed using extruder and build plate temperatures based on supplier recommendations and all other settings were consistent across materials. The

single-walled VM cylinders were chosen due to the "printer-friendly" nature of the structure, simple thermal history, and the ability to print with fibers oriented perpendicular to the testing direction. Solid and porous compression samples were printed with PEKK. All samples were printed using an Aon M2 Industrial 3D printer and the filaments were dried in an oven to remove moisture at 150°C for at least 4 hours. The solid tensile samples and porous compression cylinders were sliced using Simplify3D slicing software while the solid and porous compression samples were sliced using PrusaSlicer software due to the unavailability of the 3-dimensional gyroid infill pattern in the Simplify3D software.

Solid Tensile samples

Both dogbones and VM cylinders were printed at 70°C and 130°C build chamber temperatures (Tch) for all materials (PEEK, PEKK, and PPSU). These chamber temperatures were the lowest and highest values based on the printer's capabilities. All other print parameters were kept constant. The dogbone samples were D638 type V dogbones with a 3mm thickness and printed flat in the XY plane on the build plate so that printed fibers were parallel to tensile testing direction (Figure 27a-b). The single-walled VM cylinders were printed upright using a spiralized "vase-mode" toolpath so that printed fibers were perpendicular to tensile testing direction (Figure 27c-d). The cylinders were 70 mm tall with a 11.5 mm diameter and a 0.72 mm wall thickness (based on the extrusion width print parameter). For tensile testing, the ends of the open

cylinder were reinforced with an epoxy (SigWong, China) tab to create a solid grip section. A silicone mold (Diamond Driven Liquid Silicone Compound) with the desired epoxy tab dimensions was created. For annealed PEKK, an epoxy tab with an additional length of 5 mm was used because samples with initial dimensions broke prematurely in the epoxy section due to shearing between epoxy and printed cylinder. The silicone mold was filled with epoxy resin, VM cylinders were placed upright in the mold and the mold was placed in an oven at 60°C for 3 hours to cure the epoxy. A hole was drilled in the cured epoxy to allow air to escape and the procedure was then repeated on the other side to create epoxy tabs on both sides of the sample.

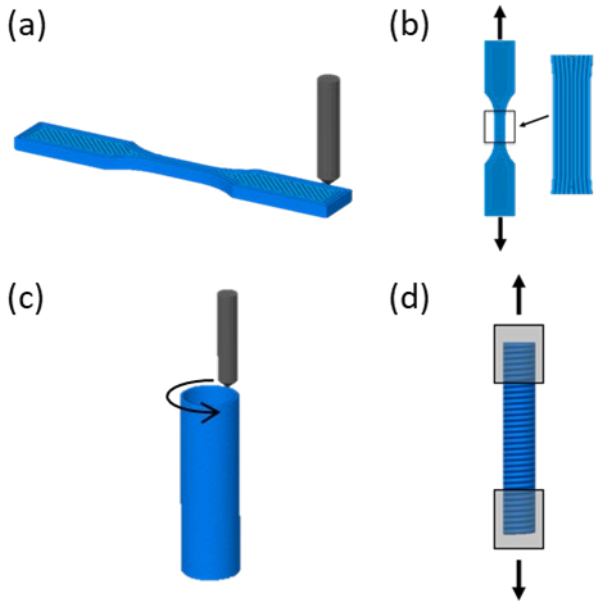

Figure 27: Printing orientation and testing schematic for D638 Type V dogbones in flat print orientation (a) that are tensile tested with printed fibers parallel to direction of loading (b), hollow cylinder that is printed in "vase mode" (VM) (c) with reinforced epoxy ends for tensile testing with printed fibers perpendicular to direction of loading (d)

5.2.2 Post process annealing

After printing, PEKK solid dogbones and VM cylinders printed in 70°C chamber temperature were annealed at 160°C (below T_{cc}) and 200°C (above T_{cc}) for 12 hours. To minimize warping, dogbones were placed between two metal plates and rolled aluminum foil rods were placed inside VM cylinders. The glass transition temperature (T_g) of the PEKK filament is 153°C, as measured with differential scanning calorimetry (DSC). A heating rate of 20°C/min and the second heat pass of a heat – cool – heat cycle was used to determine T_g. The anneal temperatures of 160°C and 200°C were determined to be below/above T_{cc} through experimentally annealing samples and measuring crystallinity with DSC.

5.2.3 Differential scanning calorimetry

The crystallinity of PEKK printed samples, as printed and annealed, was determined using DSC (TA Discovery 2500). Approximately 10 mg was cut from the dogbone and VM cylinder samples and heated at 10°C/min in a nitrogen environment. The percent crystallinity was determined from the first pass ΔH_m minus ΔH_{cc} and divided by the theoretical $\Delta H_{100\%}$ of 130 J/g for 100% crystalline PEKK[42], [62], *Equation 1*. Calibration was performed with an Indium standard.

Equation 1. Formula for calculation of crystallinity percentage of samples

$$\chi_c = \frac{\Delta H_m - \Delta H_{cc}}{\Delta H_{100\%}} \times 100$$

5.2.4 Monotonic tensile testing

The engineering stress-strain behavior of the printed dogbones and VM cylinders was determined through monotonic tensile testing (Test Resources 830EL63 and MTS Exceed® Electromechanical Test System). Dogbones and VM cylinders were tested at a displacement rate of 1 mm/min until failure. Failure is defined as the fracture of one or all of the printed fibers in the sample resulting in a decrease in stress. The cross-section dimensions of samples were measured with calipers before testing. Strain for the dogbones was measured by marking tracking points on the sample before testing and using a video extensometer system. Strain for the VM cylinders was calculated based on the distance between the epoxy reinforced sections and displacement of the crosshead.

5.2.5 Tensile fatigue testing

Tensile fatigue tests were run on a Test Resources The Nano Plug and Play machine at a frequency of 1 Hz with a sinusoidal load and an R-value of 0.1. PEKK as printed and annealed samples were tested at increasingly lower stresses below the ultimate monotonic tensile stress of the samples to generate S-N curves and determine the endurance limits of the respective samples. Samples were measured with calipers before testing to determine the force range for each samples' fatigue test. Tests were run until failure or runout. Runout was defined as greater than 1,000,000 cycles unless noted otherwise.

5.3 Results and Discussion

5.3.1 Crystallinity and tensile properties of as-printed samples

The crystallinity of the printed samples was dependent on sample geometry and build chamber temperature, Table VIII. Crystallinity was only measured for PEKK samples as PPSU is an amorphous material. The highest crystallinity of as-printed PEKK samples was 9.5%. Both PEKK dogbones had low crystallinity <2% while the PEKK VM cylinder had low crystallinity in a 70°C chamber temperature (0.9%) and a higher crystallinity of 9.5% in a 130°C chamber temperature. All PEKK as-printed samples went through cold crystallization during DSC, indicating that the samples had not reached maximum crystallinity as-printed.

Table VIII: DSC thermal properties of PEKK as-printed samples including average and standard deviation, n = 3

Material	Sample Geometry	Build Chamber Temperature T_{Ch} (°C)	Cold crystallization peak temperature, T_{cc} (°C)	Cold crystallization enthalpy, ΔH_{cc} (J/g)	Melt temperature, T_m (°C)	Total enthalpy, ΔH (J/g)	Crystalline fraction, χ_c (%)
PEKK	Dogbone	70	207 ± 1.1		335 ± 1.1	1.5 ± 0.3	1.2 ± 0.2
		130	209 ± 1.2		335 ± 1.7	1.9 ± 0.8	1.5 ± 0.7
	VM cylinder	70	206 ± 0.2		334 ± 0.2	1.2 ± 0.8	0.9 ± 0.6
		130	205 ± 0.3		334 ± 0.2	12.4 ± 1.2	9.5 ± 0.9

The tensile behavior of the samples was also dependent on material, sample geometry and build chamber temperature, Table IX. For PEKK, there was not a significant difference in the UTS in different build chamber temperatures for each of the

sample geometries, but there were differences in the failure strain. The PEKK dogbone samples had a larger strain at failure (0.53 mm/mm) in a higher build chamber temperature than the dogbones printed in a lower build chamber temperature (0.41 mm/mm), Figure 28a. This trend switched for the PEKK VM cylinder samples where the lower build chamber temperature samples had a higher failure strain (0.12 mm/mm) than the higher build chamber temperature (0.07 mm/mm), Figure 28c. The PPSU dogbones had a similar failure stress and strain (Figure 28b) while the VM cylinder - 130°C had a higher failure stress and strain than the VM cylinder - 70°C, Figure 28d.

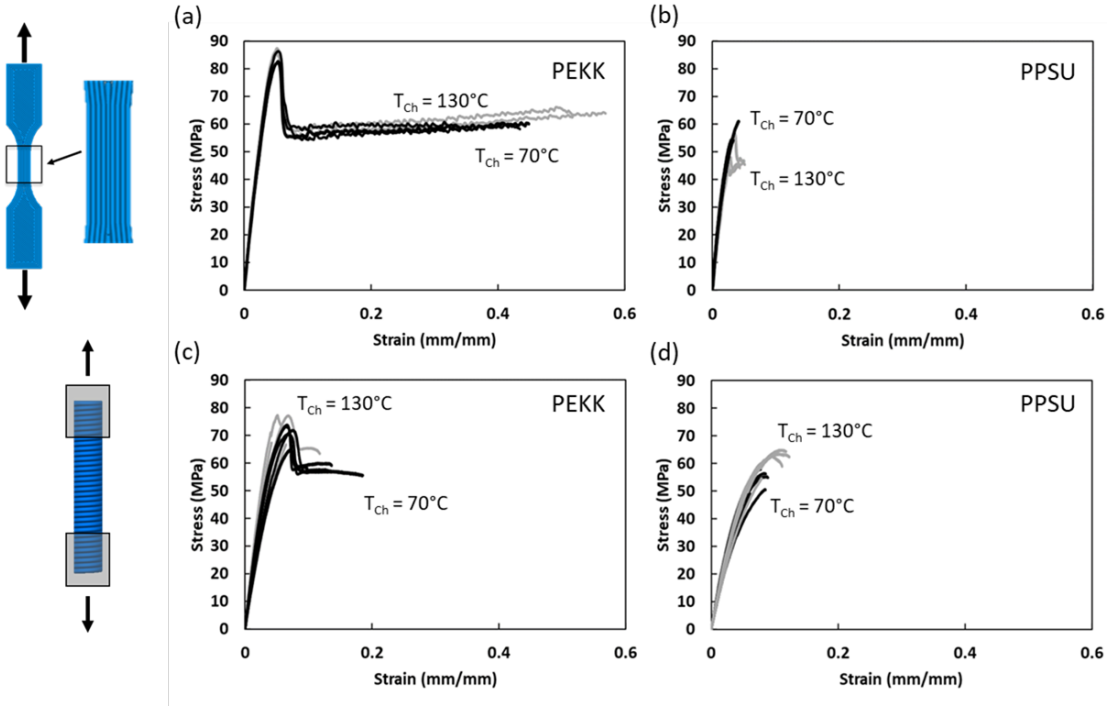

Figure 28: PEKK and PPSU tensile stress-strain curves for D638 Type V dogbones printed in a 70°C chamber temperature (black) and 130°C chamber temperature (gray) with PEKK (a) and PPSU (b) and tensile stress-strain curves for VM cylinders printed in a 70°C chamber temperature (black) and 130°C chamber temperature (gray) with PEKK (c) and PPSU (d)

For PEKK, the dogbones with fibers oriented parallel to the testing direction had higher UTS than the VM cylinder (fibers perpendicular to testing direction), Table IX, similar to findings for PEEK in Section 4.3.4. Unexpectedly, PPSU VM cylinders (T_{Ch} = 130°C) had a higher UTS than the dogbones (T_{Ch} = 130°C). However, these dogbones broke prematurely, outside the gauge section of the dogbone. Overall, PEKK had the highest UTS and strain at failure for both sample geometries compared to PPSU and PEEK.

Table IX: Tensile strength for PPSU and PEKK from dogbone and VM cylinder geometries with DSC crystallinity of samples

Material	Sample geometry	Chamber temperature (°C)	Average UTS ± StDev (MPa)	Failure strain ± StDev (mm/mm)	Crystallinity ± StDev (%)
PPSU	Dogbone	70	56.5 ± 3.9	0.03 ± 0.01	--
	n = 3	130	50.4± 5.2	0.05 ± 0.01	--
	VM cylinder	70	50.1 ± 10	0.07 ± 0.02	--
	n = 6	130	61.2 ± 4.1	0.11 ± 0.02	--
PEKK	Dogbone	70	83.7 ± 2.3	0.41 ± 0.06	1.2 ± 0.2
	n = 3	130	86.3 ± 1.5	0.53 ± 0.05	1.5 ± 0.7
	VM cylinder	70	70.2 ± 3.7	0.12 ± 0.04	0.9 ± 0.6
	n = 6	130	68.4 ± 12	0.07 ± 0.03	9.5 ± 0.9

5.3.2 Annealing of PEKK

As PEKK-70°C samples printed with a low crystallinity, samples were annealed below and above cold crystallization at 160°C and 200°C, respectively. Annealed dogbones were stronger and less ductile than as-printed samples, Figure 29 and Figure 30.

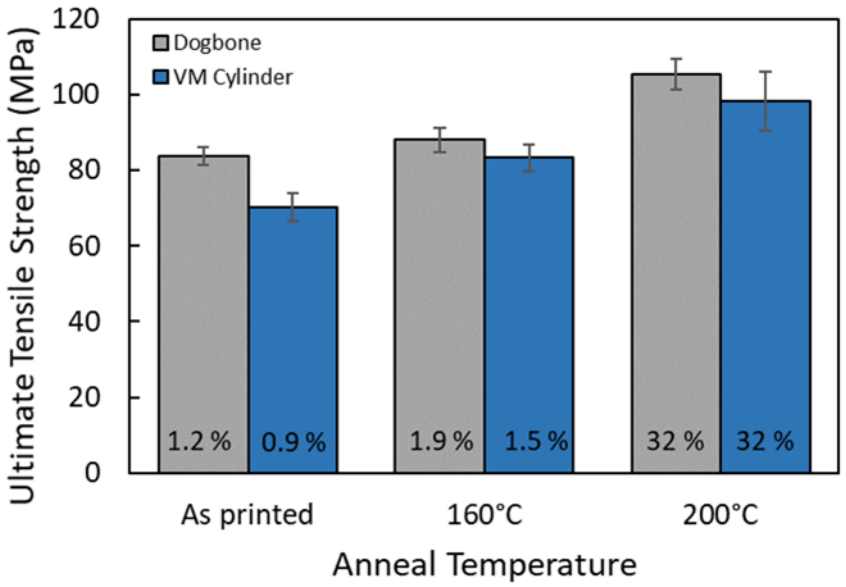

Figure 29: Chart of UTS of PEKK dogbones and VM cylinders as-printed (T_{Ch} = 70°C) and annealed at 160°C for 12 hours and 200°C for 12 hours with the respective average DSC crystallinity for each sample inset on the bar.

The dogbones annealed at 160°C had a slightly higher UTS (88 MPa) and crystallinity (1.9%) and they still underwent cold crystallization during the DSC procedure, indicating they were not fully crystalline. While the strength increased, the strain at failure decreased to 0.3 mm/mm, Figure 30a. The dogbones annealed at 200°C had a crystallinity of 32% and did not cold crystallize during DSC, indicating they had reached full crystallinity. The UTS increased 26% from 83.7 MPa for the as-printed sample to 105.4 MPa for the 200°C annealed dogbone and the strain at failure decreased further to 0.05 mm/mm, Figure 30b. UTS of annealed VM cylinders increased from 70.2 MPa as-printed to 83.3 MPa 160°C annealed and 98.3 MPa 200°C annealed, a 40% increase in strength, Figure 29. The stress-strain curves, Figure 30c-d, show an increase

in strain at failure; however, changes to the epoxy tab dimensions could be the cause as strain calculations for the VM cylinders were based on the crosshead displacement and the distance between the epoxy for each sample.

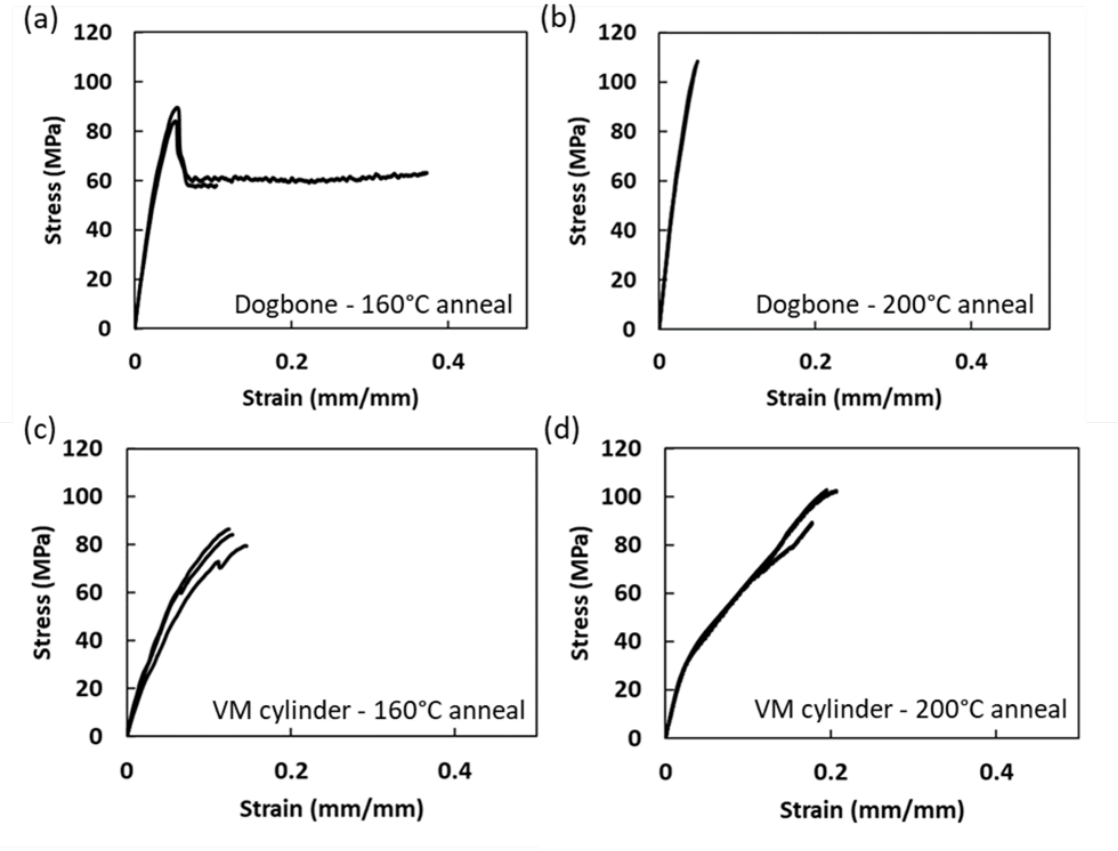

Figure 30: Tensile stress-strain curves for PEKK-70°C dogbones annealed at 160°C for 12 hours (a), annealed at 200°C for 12 hours (b) and PEKK-70°C VM cylinders annealed at 160°C for 12 hours (c), annealed at 200°C for 12 hours (d)

5.3.3 Tensile fatigue of PEKK

Tensile fatigue tests were run for as-printed and annealed PEKK (T_{Ch}=70°C) samples, Figure 31. While as-printed dogbones had higher monotonic tensile strength than the as-printed VM cylinder, the fatigue life at one million cycles of the VM cylinder

was 30 MPa which matched the dogbone. The annealed dogbone sample showed an improvement in properties, as it did with monotonic tensile strength, with a fatigue life at one million cycles of 40 MPa compared to 30 MPa for the as-printed dogbone. However, when normalized to its monotonic UTS (Figure 31b), there was only a slight improvement from 36% of UTS as-printed to 38% of UTS annealed.

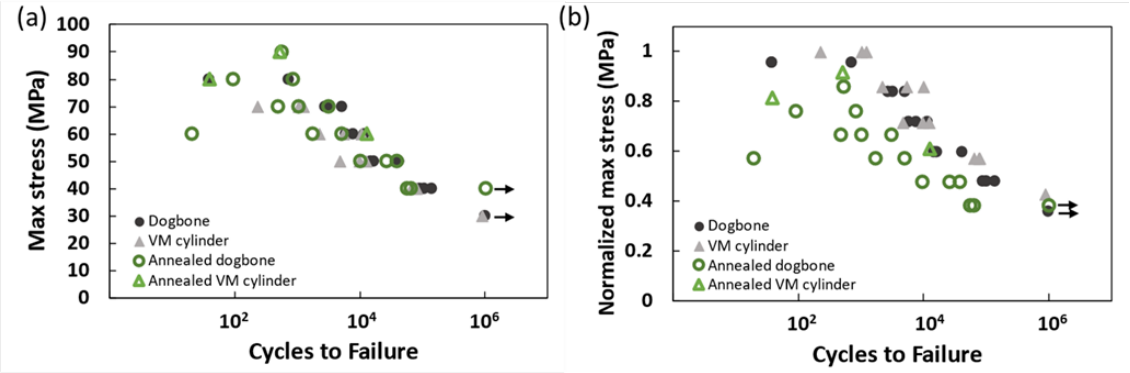

Figure 31: S-N curves of as-printed and annealed (200°C for 12 hours) PEKK (T_{CH}=70°C) samples compared to the max stress of the fatigue cycle (a) and the max stress normalized to the average monotonic UTS for each sample (b). Arrows denote samples that were stopped once they reached predetermined runout of 10^6 cycles

When normalized to monotonic UTS, the VM cylinder had the best fatigue properties, though at 43% of its UTS, it only reached 902,230 cycles instead of one million. There is no report of injection molded PEKK fatigue life properties, but all samples had lower fatigue life compared to injection-molded PEEK with a 81.7 MPa fatigue life at one million cycles[54].

5.4 Conclusions

While PEEK is currently the most common high-performance thermoplastic, both in medical device application and 3D printing literature, current understanding shows that crystallization during printing limits weld formation and mechanical properties. Further investigation into the control of PEEK crystallization during printing may enable better properties in PEEK, however, PEKK and PPSU are alternative materials that are more suited to FFF 3D printing due to their low crystallinity during processing. PPSU samples reached strength (61 MPa) closest to injection molded strength of 70 MPa. PEKK had the highest tensile strength and strain to failure for both sample geometries, a dogbone with printed fibers parallel to testing direction and a cylinder with fibers perpendicular to testing direction. As-printed PEKK samples had low crystallinity and annealing fully crystallized the samples and increased the tensile strength by 26-40% with an ultimate tensile strength of 98 MPa and 105 MPa, for the cylinder and dogbone geometries respectively.

6. Conclusions

This research covered multiple materials to evaluate the relationship between their structure and properties when FFF processed. PLA, PEEK, PEKK and PPSU thermoplastics were selected for investigation due to their high strength, relevance in implantable orthopedic devices, and capability for FFF processing. The focus of this research was to characterize their FFF properties and determine areas for improvement with a focus on the welds that form between layers during FFF processing. Print processing and post process annealing parameters were analyzed to determine impact on the structure and properties of printed parts.

First, with PLA, annealing was explored as a potential post-processing method to improve strength at the weld, after confirming that the print orientation and direction of fibers in respect to loading have the largest impact on mechanical properties in FFF materials due to weaknesses at the weld. Annealing above T_{cc} increased crystallinity, while having minimal impact on porosity. However, while crystallinity increased tensile strength in injection molded PLA, strength of FFF PLA either decreased or remained constant, suggesting that co-crystallization across the weld does not occur. AFM images support this finding showing weld interfaces between printed fibers are still visible after annealing above T_{cc}. During annealing, spherulites grow into the bulk of the fiber instead of across the weld interface. Importantly, annealing below T_{cc} shows a moderate but significant increase in tensile strength, while not impacting porosity or crystallinity.

AFM images show that the as-printed interface between fibers is not fully cohesive but annealing below T_{cc} heals the as-printed interface resulting in an increase in tensile strength. While annealing has some promise for improving strength at the weld, more research is needed on the formation of the weld and improving fiber coalescence to improve the mechanical properties of FFF PLA and decrease anisotropy between printing directions. The understanding that increasing the crystallinity could create more brittle materials informed the experimental design for investigating PEEK.

PEEK has long been an attractive material for the additive manufacturing of medical implants due to its exceptional mechanical properties and chemical inertness. However, PEEK components manufactured via fused filament fabrication have suffered from poor mechanical properties and anisotropy due to poor weld strength. Tearing energy measurements of FFF-PEEK samples printed at different chamber temperatures indicate that increased crystallinity in the printed PEEK decreases weld strength, contrary to expectations from bulk mechanical property behavior.

From AFM imaging of the weld zone in FFF-PEEK, we hypothesize that the crystallinity at the interface is the result of surface induced crystallization that prevents strong weld formation between FFF-PEEK filaments. One possible mechanism for the high surface is crystallinity is free surface effects. At the free surface, higher polymer mobility is observed, resulting in a reduction of local Tg and Tcc and an increase in the crystallization kinetics. During deposition of the PEEK filaments, free-surface mediated

crystallization allows rapid formation of PEEK crystallites in the surface layer of the deposited filament faster than what is expected from bulk measurements of crystallization from DSC. As a result, the free surface of the deposited filament crystallizes before the next layer can be deposited. The crystallized surface layer of polymer forms a hard, immobile 'skin' that prevents weld formation between the printed layers. Therefore, the reduction of fracture toughness with increased crystallinity is expected. To address the surface crystallization the print geometry and chamber temperature is adjusted such that amorphous PEEK parts are printed. Two-step annealing, where the printed part is first annealed above Tg, but below the Tcc allows for relaxation of non-equilibrium conformations and weld healing without crystallization followed by a second annealing step above Tcc to induce cold crystallization, yields fully crystalline FFF-PEEK parts with 6-8× stronger welds than what is achieved with standard printing methods. Further investigation is required to determine appropriate annealing times for weld healing from the polymer rheology and diffusion kinetics between Tg and Tcc. Additionally, the results in the bulk tensile samples, and improvement of UTS with the high build chamber temperature VM cylinder, warrant further investigation into slowing crystallization and improving polymer chain diffusion across the weld by raising the temperature of printed material closer to the melt either through a printer with a higher build chamber temperature (global temperature control) or through local temperature control at the hotend.

While PEEK is currently the most common high-performance thermoplastic, both in medical device application and 3D printing literature, current understanding shows that fast crystallization during printing limits weld formation and mechanical properties. Further investigation into the control of PEEK crystallization during printing may enable better properties in PEEK. However, PEKK and PPSU are alternative materials that are more suited to FFF 3D printing due to their low crystallinity during processing. PPSU samples reached strength (61 MPa) closest to injection molded strength of 70 MPa. PEKK had the highest tensile strength and strain to failure for both sample geometries, a dogbone with printed fibers parallel to testing direction and a cylinder with fibers perpendicular to testing direction. As-printed PEKK samples had low crystallinity and annealing fully crystallized the samples and increased the tensile strength by 26-40% with an ultimate tensile strength of 98 MPa and 105 MPa, for the VM cylinder and dogbone geometries respectively.

References

[1] W. D. Callister, "Materials science and engineering: An introduction (2nd edition)," *Mater. Des.*, 1991.

[2] I. V. Panayotov, V. Orti, F. Cuisinier, and J. Yachouh, "Polyetheretherketone (PEEK) for medical applications," *Journal of Materials Science: Materials in Medicine*. 2016.

[3] S. Kurtz, *PEEK Biomaterials Handbook*. 2012.

[4] J.-W. Tseng *et al.*, "Screw extrusion-based additive manufacturing of PEEK," *Mater. Des.*, vol. 140, pp. 209–221, Feb. 2018.

[5] "OsteoFab® Implants | OPM." [Online]. Available: http://oxfordpm.com/cmf-orthopedics/osteofab-implants. [Accessed: 07-Dec-2018].

[6] S. C. Ligon, R. Liska, J. Stampfl, M. Gurr, and R. Mülhaupt, "Polymers for 3D Printing and Customized Additive Manufacturing," *Chemical Reviews*, vol. 117, no. 15. 2017.

[7] A. Das *et al.*, "Current understanding and challenges in high temperature additive manufacturing of engineering thermoplastic polymers," 2020.

[8] B. C. Gross, J. L. Erkal, S. Y. Lockwood, C. Chen, and D. M. Spence, "Evaluation of 3D printing and its potential impact on biotechnology and the chemical sciences," *Anal. Chem.*, vol. 86, no. 7, pp. 3240–3253, 2014.

[9] "EOS P 810 - High-temperature polymer laser sintering." [Online]. Available: https://www.eos.info/systems_solutions/eos-p-810. [Accessed: 02-Apr-2020].

[10] S. Dadbakhsh, L. Verbelen, O. Verkinderen, D. Strobbe, P. Van Puyvelde, and J. P. Kruth, "Effect of PA12 powder reuse on coalescence behaviour and microstructure of SLS parts," *Eur. Polym. J.*, vol. 92, pp. 250–262, Jul. 2017.

[11] A. M. Forster, "Materials Testing Standards for Additive Manufacturing of Polymer Materials: State of the Art and Standards Applicability."

[12] D. Popescu, A. Zapciu, C. Amza, F. Baciu, and R. Marinescu, "FDM process parameters influence over the mechanical properties of polymer specimens: A review," *Polym. Test.*, vol. 69, pp. 157–166, Aug. 2018.

[13] O. A. Mohamed, • Syed, H. Masood, and J. L. Bhowmik, "Optimization of fused deposition modeling process parameters: a review of current research and future prospects."

[14] J. E. Seppala, S. Hoon Han, K. E. Hillgartner, C. S. Davis, and K. B. Migler, "Weld formation during material extrusion additive manufacturing," *Soft Matter*, vol. 13, no. 38, pp. 6761–6769, 2017.

[15] A. A. D'Amico, A. Debaie, and A. M. Peterson, "Effect of layer thickness on irreversible thermal expansion and interlayer strength in fused deposition modeling," *Rapid Prototyp. J.*, vol. 23, no. 5, pp. 943–953, 2017.

[16] S. A. Tronvoll, T. Welo, and C. W. Elverum, "The effects of voids on structural properties of fused deposition modelled parts: a probabilistic approach," *Int. J. Adv. Manuf. Technol.*, vol. 97, no. 9–12, pp. 3607–3618, Aug. 2018.

[17] C. Mcilroy, J. E. Seppala, and A. P. Kotula, "Combining Modeling and Measurements To Predict Crystal Morphology in Material Extrusion," *Polym. Addit. Manuf. Recent Dev. Part 6 - Comb. Model. Meas. To Predict Cryst. Morphol. Mater. Extrus.*, 2019.

[18] Y. S. Ko, D. Herrmann, O. Tolar, W. J. Elspass, and C. Brändli, "Improving the filament weld-strength of fused filament fabrication products through improved interdiffusion," *Addit. Manuf.*, 2019.

[19] T. J. Coogan and D. O. Kazmer, "Prediction of interlayer strength in material extrusion additive manufacturing," *Addit. Manuf.*, vol. 35, Oct. 2020.

[20] L. A. Northcutt, S. V. Orski, K. B. Migler, and A. P. Kotula, "Effect of processing conditions on crystallization kinetics during materials extrusion additive manufacturing," *Polymer (Guildf).*, vol. 154, pp. 182–187, Oct. 2018.

[21] Y. Liao *et al.*, "Effect of porosity and crystallinity on 3D printed PLA properties," *Polymers (Basel).*, vol. 11, no. 9, Sep. 2019.

[22] R. A. Wach, P. Wolszczak, and A. Adamus-Wlodarczyk, "Enhancement of Mechanical Properties of FDM-PLA Parts via Thermal Annealing," *Macromol. Mater. Eng.*, vol. 303, no. 9, p. 1800169, Sep. 2018.

[23] V. Srinivas, C. S. J. van Hooy-Corstjens, and J. A. W. Harings, "Correlating molecular and crystallization dynamics to macroscopic fusion and thermodynamic stability in fused deposition modeling; a model study on

polylactides," *Polymer (Guildf).*, vol. 142, pp. 348–355, Apr. 2018.

[24] Y.-Q. Xue, T. A. Tervoort, ‡ S Rastogi, and P. J. Lemstra, "Welding Behavior of Semicrystalline Polymers. 2. Effect of Cocrystallization on Autoadhesion," 2000.

[25] Y. Song, Y. Li, W. Song, K. Yee, K.-Y. Lee, and V. L. Tagarielli, "Measurements of the mechanical response of unidirectional 3D-printed PLA," *Mater. Des.*, vol. 123, pp. 154–164, Jun. 2017.

[26] C. Basgul, T. Yu, D. W. Macdonald, R. Siskey, M. Marcolongo, and S. M. Kurtz, "Does annealing improve the interlayer adhesion and structural integrity of FFF 3D printed PEEK lumbar spinal cages?," 2019.

[27] J. Torres, J. Cotelo, J. Karl, and A. P. Gordon, "Mechanical Property Optimization of FDM PLA in Shear with Multiple Objectives," *JOM*, vol. 67, no. 5, pp. 1183–1193, May 2015.

[28] L. Wang, W. M. Gramlich, and D. J. Gardner, "Improving the impact strength of Poly(lactic acid) (PLA) in fused layer modeling (FLM)," *Polymer (Guildf).*, vol. 114, pp. 242–248, Apr. 2017.

[29] C. Yang, X. Tian, D. Li, Y. Cao, F. Zhao, and C. Shi, "Influence of thermal processing conditions in 3D printing on the crystallinity and mechanical properties of PEEK material," *J. Mater. Process. Technol.*, vol. 248, no. May, pp. 1–7, 2017.

[30] C. Basgul, T. Yu, D. W. MacDonald, R. Siskey, M. Marcolongo, and S. M. Kurtz, "Structure–property relationships for 3D-printed PEEK intervertebral lumbar cages produced using fused filament fabrication," *J. Mater. Res.*, vol. 33, no. 14, pp. 2040–2051, Jul. 2018.

[31] J. Beniak, P. Križan, M. Matúš, and M. Šajgalík, "Experimental testing of PLA biodegradable thermoplastic in the frame of 3D printing FDM technology," in *MATEC Web of Conferences*, 2018, vol. 157.

[32] O. Luzanin, V. Guduric, I. Ristic, and S. Muhic, "Investigating impact of five build parameters on the maximum flexural force in FDM specimens - A definitive screening design approach," *Rapid Prototyp. J.*, vol. 23, no. 6, pp. 1088–1098, 2017.

[33] L. Yang, S. Li, Y. Li, M. Yang, and Q. Yuan, "Experimental Investigations for Optimizing the Extrusion Parameters on FDM PLA Printed Parts," *J. Mater. Eng. Perform.*, vol. 28, no. 1, pp. 169–182, Jan. 2019.

[34] S. R. Rajpurohit and H. K. Dave, "Analysis of tensile strength of a fused filament fabricated PLA part using an open-source 3D printer," *Int. J. Adv. Manuf. Technol.*, vol. 101, no. 5–8, pp. 1525–1536, Apr. 2019.

[35] S. R. Rajpurohit and H. K. Dave, "Effect of process parameters on tensile strength of FDM printed PLA part," *Rapid Prototyp. J.*, vol. 24, no. 8, pp. 1317–1324, 2018.

[36] J. E. Seppala, S. Hoon Han, K. E. Hillgartner, C. S. Davis, and K. B. Migler, "Weld formation during material extrusion additive manufacturing," *Soft Matter*, vol. 13, no. 38, pp. 6761–6769, 2017.

[37] H. Li, T. Wang, Q. Li, Z. Yu, and N. Wang, "A quantitative investigation of distortion of polylactic acid/PLA) part in FDM from the point of interface residual stress," *Int. J. Adv. Manuf. Technol.*, vol. 94, no. 1–4, pp. 381–395, Jan. 2018.

[38] F. Carrasco, P. Pagès, J. Gámez-Pérez, O. O. Santana, and M. L. Maspoch, "Processing of poly(lactic acid): Characterization of chemical structure, thermal stability and mechanical properties," *Polym. Degrad. Stab.*, vol. 95, no. 2, pp. 116–125, Feb. 2010.

[39] J. M. Chacón, M. A. Caminero, E. García-Plaza, and P. J. Núñez, "Additive manufacturing of PLA structures using fused deposition modelling: Effect of process parameters on mechanical properties and their optimal selection," *Mater. Des.*, vol. 124, pp. 143–157, Jun. 2017.

[40] E. W. Fischer, H. J. Sterzel, and G. Wegner, "Investigation of the structure of solution grown crystals of lactide copolymers by means of chemical reactions," *Kolloid-Zeitschrift Zeitschrift für Polym.*, vol. 251, no. 11, pp. 980–990, Nov. 1973.

[41] T. J. Coogan and D. O. Kazmer, "Healing simulation for bond strength prediction of FDM," *Rapid Prototyp. J.*, vol. 23, no. 3, pp. 551–561, 2017.

[42] D. J. Blundell and B. N. Osborn, "The morphology of poly(aryl-ether-ether-ketone)," *Polymer (Guildf).*, vol. 24, no. 8, pp. 953–958, Aug. 1983.

[43] J. E. Seppala, S. Hoon Han, K. E. Hillgartner, C. S. Davis, and K. B. Migler, "Weld formation during material extrusion additive manufacturing," *Soft Matter*, vol. 13, no. 38, pp. 6761–6769, 2017.

[44] J. Pu, C. McIlroy, A. Jones, and I. Ashcroft, "Understanding Mechanical Properties in Fused Filament Fabrication of Polyether Ether Ketone," *Addit. Manuf.*, p. 101673, Oct. 2020.

[45] S. Luo *et al.*, "Interplay between Free Surface and Solid Interface Nucleation on Two-Step Crystallization of Poly(ethylene terephthalate) Thin Films Studied by Fast Scanning Calorimetry," *Macromolecules*, 2018.

[46] K. Taguchi, H. Miyaji, K. Izumi, A. Hoshino, Y. Miyamoto, and R. Kokawa, "Crystal growth of isotactic polystyrene in ultrathin films: Film thickness dependence," *J. Macromol. Sci. - Phys.*, 2002.

[47] A. M. Gohn, J. Seo, R. H. Colby, R. P. Schaake, R. Androsch, and A. M. Rhoades, "Crystal nucleation in poly(ether ether ketone)/carbon nanotube nanocomposites at high and low supercooling of the melt," *Polymer (Guildf).*, 2020.

[48] W. Wang, J. M. Schultz, and B. S. Hsiao, "Dynamic Study of Crystallization-and Melting-Induced Phase Separation in PEEK/PEKK Blends," 1997.

[49] R. Chivers, "The effect of molecular weight and crystallinity on the mechanical properties of injection moulded poly(aryl-ether-ether-ketone) resin," *Polymer (Guildf).*, vol. 35, no. 1, pp. 110–116, Jan. 1994.

[50] S. M. Kurtz and J. N. Devine, "PEEK biomaterials in trauma, orthopedic, and spinal implants.," *Biomaterials*, vol. 28, no. 32, pp. 4845–69, Nov. 2007.

[51] L. Martineau, F. Chabert, B. Boniface, and G. Bernhart, "Effect of interfacial crystalline growth on autohesion of PEEK," *Int. J. Adhes. Adhes.*, vol. 89, pp. 82–87, Mar. 2019.

[52] M. C. Sobieraj, S. M. Kurtz, and C. M. Rimnac, "Notch sensitivity of PEEK in monotonic tension," *Biomaterials*, 2009.

[53] H. Motz and J. M. Schultz, "The Solidification of PEEK. Part II: Kinetics."

[54] N. T. Evans, C. W. Irvin, D. L. Safranski, and K. Gall, "Impact of surface porosity and topography on the mechanical behavior of high strength biomedical polymers," *J. Mech. Behav. Biomed. Mater.*, vol. 59, pp. 459–473, Jun. 2016.

[55] A. E. M. Eltorai, E. Nguyen, and A. H. Daniels, "Three-Dimensional Printing in Orthopedic Surgery," *Orthopedics*, vol. 38, no. 11, pp. 684–687, 2015.

[56] V. R. Sastri, *Plastics in Medical Devices: Properties, Requirements, and Applications: Second Edition*. 2013.

[57] D. K. Platt and Rapra Technology Limited., *Engineering and high performance*

plastics market report : a Rapra market report. 2003.

[58] V. Kishore *et al.*, "Rheological characteristics of fiber reinforced Poly (Ether Ketone Ketone) (PEKK) for melt extrusion additive manufacturing," *Int. SAMPE Tech. Conf.*, pp. 1783–1791, 2017.

[59] M. Arifa, S. Kumar, K. M. Varadarajanb, and W. J. Cantwell, "Performance of Biocompatible PEEK Processed by Fused Deposition Additive Manufacturing," *Mater. Des. Manuscr.*

[60] M. Rinaldi, T. Ghidini, F. Cecchini, A. Brandao, and F. Nanni, "Additive layer manufacturing of poly (ether ether ketone) via FDM," *Compos. Part B Eng.*, vol. 145, no. December 2017, pp. 162–172, 2018.

[61] L. M. Ricles, J. C. Coburn, M. Di Prima, and S. S. Oh, "Regulating 3D-printed medical products.," *Sci. Transl. Med.*, vol. 10, no. 461, p. eaan6521, Oct. 2018.

[62] T. Choupin *et al.*, "Influence of thermal history on the mechanical properties of poly(ether ketone ketone) copolymers," *Polym. Cryst.*, vol. 2, no. 6, pp. 1–8, Dec. 2019.